Examination of Surface Wind Asymmetries in Tropical Cyclones. Part I: General Structure and Wind Shear Impacts

BRADLEY W. KLOTZ

Cooperative Institute for Marine and Atmospheric Studies, Rosenstiel School of Marine and Atmospheric Science, University of Miami, and NOAA/AOML/Hurricane Research Division, and Department of Earth and Environment, Florida International University, Miami, Florida

HAIYAN JIANG

Department of Earth and Environment, Florida International University, Miami, Florida

(Manuscript received 30 January 2017, in final form 6 July 2017)

ABSTRACT

Because surface wind speeds within tropical cyclones are important for operational and research interests, it is vital to understand surface wind structure in relation to various storm and environmental influences. In this study, global rain-corrected scatterometer winds are used to quantify and evaluate characteristics of tropical cyclone surface wind asymmetries using a modified version of a proven aircraft-based low-wavenumber analysis tool. The globally expanded surface wind dataset provides an avenue for a robust statistical analysis of the changes in structure due to tropical cyclone intensity, deep-layer vertical wind shear, and wind shear's relationship with forward storm motion. A presentation of the quantified asymmetry indicates that wind shear has a significant influence on tropical storms at all radii but only for areas away from the radius of maximum wind in both nonmajor and major hurricanes. Evaluation of a shear's directional relation to motion indicates that a cyclonic rotation of the surface wind field asymmetry from downshear left to upshear left occurs in conjunction with an anticyclonic rotation of the directional relationship (i.e., from shear direction to the left, same, right, or opposite of the motion direction). It was discovered that in tropical cyclones experiencing effects from wind shear, an increase in absolute angular momentum transport occurs downshear and often downshear right. The surface wind speed low-wavenumber maximum in turn forms downwind of this momentum transport.

1. Introduction

Three-dimensional kinematic structure is a complicated yet important piece of the overall structure of tropical cyclones (TCs). Because people influenced and impacted by TCs experience these storms at the surface level, operational centers worldwide are required to report TC strength based on a surface wind speed. It is known that the maximum tangential wind is generally located within the boundary layer (Smith et al. 2009; Montgomery et al. 2009, 2014), but surface winds and the two-dimensional structure of those winds reveal important characteristics about the TC, thus making it vital for predicting when and how changes might occur.

Because surface wind speeds are directly connected to TC intensity, certain factors known to impact intensity should in turn impact the surface wind field structure. Large-scale environmental factors significantly contribute to a TC's ability to form, intensify, and rapidly intensify (Kaplan and DeMaria 2003; Hendricks et al. 2010; Kaplan et al. 2010). Some components, such as sea surface temperature, play a fairly obvious role in the intensification process (Gray 1979; Schade and Emanuel 1999). The forward motion impact on TC intensity is also well understood and well documented in terms of synoptic-scale interactions, vorticity, and beta effect (Rossby 1948; Kuo 1969; George and Gray 1976; Jones 1977; Brand et al. 1981; Holland 1983b, 1984; Chan and Williams 1987; Fiorino and Elsberry 1989; Gonzalez et al. 2015). These impacts are supported by numerical simulations (Shapiro 1983; Frank and Ritchie 1999; Thomsen et al. 2015). Intensity impact from vertical mass transport and motion (Jorgensen et al. 1985; Marks et al. 1992), along with observed precipitation or

Corresponding author: Bradley Klotz, bklotz@rsmas.miami.edu

DOI: 10.1175/MWR-D-17-0019.1

convective inner-core features, are also well documented relative to storm motion (Miller 1958; Willoughby et al. 1984; Marks 1985; Burpee and Black 1989; Franklin et al. 1993; Rodgers et al. 1994; Black et al. 1997; Corbosiero and Molinari 2003; Lonfat et al. 2004; Chen et al. 2006).

Other environmental factors, such as deep-layer vertical wind shear, are known to impact TC formation and intensification but with more variability and uncertainty compared to storm motion. Generally, increasing wind shear tends to inhibit TC formation or strengthening (Gray 1968), but there is evidence that supports TC formation and intensification in the presence of moderate-to-strong wind shear (Reasor et al. 2004; Molinari and Vollaro 2010; Reasor and Eastin 2012; Reasor et al. 2013; Rogers et al. 2015). Because vertical wind shear is variably dependent on synoptic-scale factors and on the location within a particular basin, the relationship between wind shear and storm motion has implications for determining the location and magnitude of the maximum surface wind speed (Rogers and Uhlhorn 2008; Ueno and Bessho 2011; Uhlhorn et al. 2014, hereafter U14). Additionally, vertical wind shear and storm motion significantly contribute to defining the symmetric or asymmetric structure of the boundary layer and surface wind fields (Shapiro 1983; Kepert 2001; Ueno and Kunii 2009; Zhang et al. 2013).

TC-penetrating aircraft set the standard for providing the most accurate and pertinent information needed for determining a TC's intensity (Aberson et al. 2006) as a result of observations from stepped frequency microwave radiometer (SFMR; Uhlhorn et al. 2007; Klotz and Uhlhorn 2014) and global positioning system (GPS) dropsondes (Hock and Franklin 1999; Franklin et al. 2003). When available, the observations from these instruments strongly influence the resulting ''best track'' data (Jarvinen et al. 1984; Landsea and Franklin 2013). In particular, the SFMR provides high-frequency observations of the surface winds and rain rate and is well known for producing trustworthy wind speeds within hurricanes. However, as a result of proximity or resource issues, these aircraft data are mostly collected over the North Atlantic basin and rarely over the eastern Pacific. Only ~30% of all 6-h periods over the Atlantic have aircraft data available (Rappaport et al. 2009).

Several studies have examined the viability of using microwave instrumentation (Goodberlet et al. 1989; Demuth et al. 2004, 2006; Bessho et al. 2006; Brennan et al. 2009; Knaff et al. 2011; Mai et al. 2016) and infrared imagery (Dvorak 1975; Mueller et al. 2006; Velden et al. 2006; Kossin et al. 2007) from space to obtain an estimate of the surface wind speeds in TCs. However, studies pertaining to scatterometry (Brennan et al. 2009; Stiles et al. 2010, 2014; Stiles and Dunbar 2010) provide the most direct estimation of the surface wind speeds from space. Scatterometers such as QuikSCAT (Draper and Long 2002, 2004; Hoffman and Leidner 2005) and ASCAT (Figa-Saldaña et al. 2002) have been particularly useful for determining operational wind radii, but are generally disregarded near the inner-most radii of TCs.

Scatterometer wind speeds are trustworthy up to ~30–35 m s^{-1} in TCs (Brennan et al. 2009; Stiles et al. 2014). This lack of hurricane force wind speed observation is a significant problem for TC analysis and is compounded by interference of the microwave signal from precipitation. However, it is possible to apply a correction to these wind speeds using a neural network (NN) in order to attain wind speeds up to ~55–60 m s^{-1} (±1–2 m s^{-1}; Stiles et al. 2014). While this correction method is one of several available, it was developed with the assistance of an operational product (H*WIND; Powell and Houston 1996; Powell et al. 1998) and substantially reduces the impact of precipitation on the wind speed result. Therefore, utilizing it increases the wind speed reliability in most conditions. With these improved wind speeds, more attention can be placed on the evolution of the surface wind asymmetry as it pertains to environmental and storm-specific parameters.

Several recent studies discuss surface wind structure using various methods and datasets. Ueno and Bessho (2011) examined surface wind fields using coarse scatterometer data in northwest Pacific typhoons and found a preferential left-of-shear and right-of-motion maximum wind speed. Because they used rain-flagged data, certain locations within a wind field may contain suboptimal data and could potentially call some of their results into question. Their justification for using this data was that their work was more of a ''feasibility study on the utility of the data in the TC near-core region.'' While they provide observational support for a previous study by Ueno and Kunii (2009), they only give qualitative analyses of asymmetry for a limited subset of typhoons.

Generally, the asymmetric structure is best examined using a low-wavenumber analysis as shown in U14. These authors set a foundation for observed TC surface wind structure and describe the general impact of storm motion and wind shear on the surface wind asymmetry in hurricanes. One of the main foci of U14 was the evaluation of the surface wind structure against a similar flight-level analysis, and they determined that the wavenumber-1 phase rotation due to increasing storm motion or wind shear magnitude was stronger at the surface. Because SFMR cannot provide wind direction,

it is difficult to remove the motion-induced asymmetry, but U14 attempted to use a linear regression technique for this purpose. In so doing, they provide an estimate of the wind shear impact on surface wind asymmetry, keeping in mind that the regression technique retains higher uncertainties. While U14 answers several important questions, the authors present the results for their full hurricane sample assuming that a minimal category 1 hurricane behaves similarly to a strong category 4 hurricane. Additionally, there is no examination of structure below hurricane strength because of limitations of the SFMR analysis. It would be a premature assumption to expect that tropical storm surface winds react to shear exactly like hurricanes, making it necessary to investigate these weaker TCs. The constraints of aircraft reconnaissance, however, prevent detailed examination of the full TC spectrum on a global scale.

As a way of addressing this issue with aircraft limitations, another recent study by Klotz and Jiang (2016, hereafter KJ16) presents an initial analysis of NN-corrected wind speeds on a global scale, where total surface wind speed composites relative to storm motion and wind shear are evaluated as a function of TC basin and TC intensity. The purpose of KJ16 was to provide support for theoretical studies (Shapiro 1983; Thomsen et al. 2015) using a large set of observations and to pinpoint regions of the full TC spectrum that deviate from the general downshear-left or right-of-motion wind-field orientations. Their results indicate general agreement between the basin-specific wind speed composites (with some variability) and noticeable differences in wind field orientation as a function of TC intensity. However, the composites presented only provide a qualitative analysis of the asymmetry and cannot assess the detailed impacts of wind shear, storm motion, or their interactions, which vary between the TC basins.

Because of the unanswered questions suggested by the previous surface wind studies, this present work is unique and seeks to determine the low-wavenumber, surface wind asymmetry from NN-corrected scatterometer data in a similar manner to U14 while also expanding on the initial results of KJ16. To that end, the goals of this study are 1) to provide quantified asymmetry profiles in the form of an asymmetry index as a function of TC intensity, focusing on wind regimes best obtained by the scatterometer (i.e., tropical storms and nonmajor hurricanes), 2) to more accurately determine the wind shear and motion impact on the surface wind asymmetry, and 3) to discuss potential mechanisms for certain wind shear–induced surface wind asymmetries. A data description is provided in section 2, followed by a description of the low-wavenumber method applied to the scatterometer winds in section 3. Section 4 includes results and discussion of the surface wind asymmetry as a function of TC intensity, shear, and motion angle difference, and seeks to provide an explanation for their variations. Section 5 provides conclusions to this study.

2. Data

a. Satellite-based scatterometer data

With a fairly large swath width (~1800 km for QuikSCAT), scatterometers are capable of regularly examining a TC's full wind field, which is an advantage when compared to data collected by aircraft. NASA's Jet Propulsion Laboratory (JPL) maintains a dataset (ftp://mwsci.jpl.nasa.gov/; Hristova-Veleva et al. 2013) that contains the TC-centric QuikSCAT and OceanSat Scatterometer (OSCAT) data that are available for all TC-prone basins between 2000 and 2011. The nominal (operational) resolution of these data is 25 km, but the data used in this study were processed with a horizontal resolution of 12.5 km [~1/8°; Brennan et al. (2009)]. While the scatterometer often observes a full TC wind field, lack of targeting by the satellite prevents guaranteed coverage of a TC during an overpass.

Additionally, the NN correction mentioned previously helps address the rain contamination issue for wind speeds, but there remains an uncertainty in the directional ambiguities (Stiles et al. 2014) that could have an impact on the evaluation of wind vectors. KJ16 make note of an ongoing study trying to remedy this issue, but the current wind directions could be uncertain in some locations. These uncertainties are not widespread but tend to be localized (Stiles et al. 2014; J. Zhang 2016, personal communication). All scatterometer wind speeds used herein will have the NN correction applied. Figure 1 shows an example of wind speeds from Hurricane Katrina on 28 August 2005. The uncorrected and NN wind fields are provided in the left and right panels of Fig. 1, respectively. Clearly, the maximum NN wind speeds are closer to the magnitude of the official maximum wind speed (75 m s^{-1}; Knabb et al. 2011) than those of the uncorrected winds.

b. Airborne SFMR data

To validate scatterometer winds and analyses used in this study, SFMR wind speeds and their resulting analyses are utilized. The SFMR uses a stepping technique through six C-band frequencies to determine a surface wind speed and rain rate from the six observed brightness temperatures. Data are provided at a rate of 1 Hz on a spatial scale of 1–1.5 km along track at the standard flight altitude and aircraft speed (Uhlhorn and Black 2003; Uhlhorn et al. 2007).

Despite the advantages of aircraft reconnaissance, there are also caveats that must be considered when

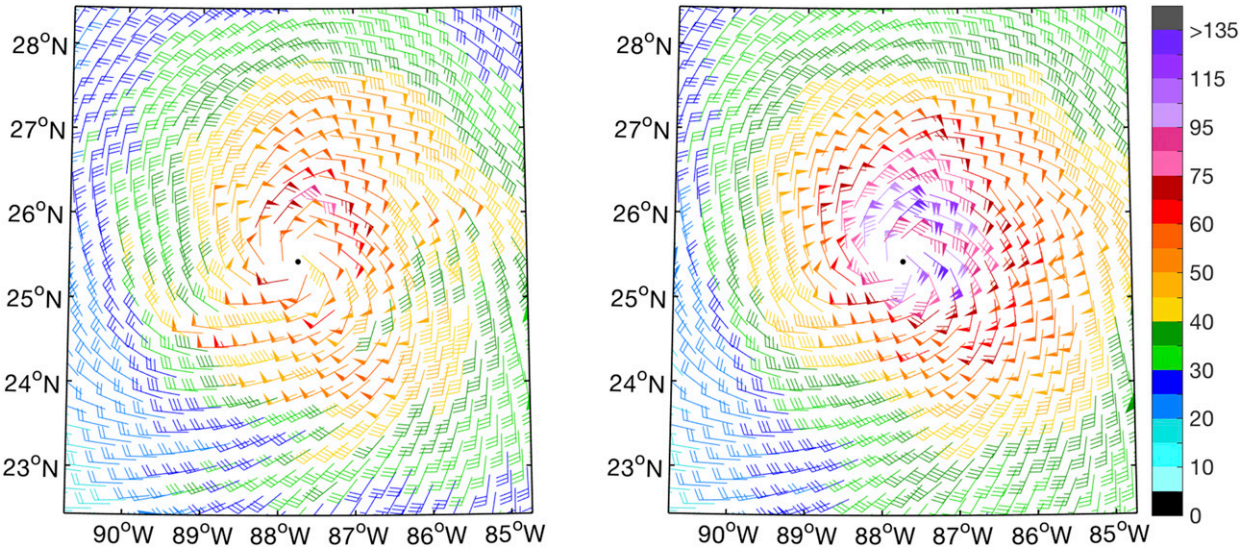

FIG. 1. QuikSCAT scatterometer surface wind barbs are shown for Hurricane Katrina on 28 Aug 2005. (left) The uncorrected wind speeds and (right) the NN-corrected wind speeds (kt, color scale, where 1 kt = 0.51 m s^{-1}) are provided. Data points are thinned by a factor of 2 to more clearly show the wind circulation. The black dot indicates the center position.

using these data. One limiting factor relates to the ability of the aircraft to sample a TC. Many TCs are out of range of the aircraft, which controls the amount of TC surface wind data that can be collected by SFMR. Another limiting factor is the SFMR high bias of wind speed in the presence of heavy rain (mostly for weaker systems). This problem has been addressed (Klotz and Uhlhorn 2014), but the SFMR data in this study have not been reprocessed with this correction. Because the cases used in U14 were hurricanes and because the SFMR performs well at high wind speeds (mean bias < 1 m s^{-1}; Klotz and Uhlhorn 2014), the lack of this bias correction will not impact the validation of the scatterometer.

c. *TC intensity, motion, and vertical wind shear data*

For TC position, official intensity, and storm motion parameters, the hurricane best-track record provides 6-hourly data and is currently available in the NHC's "best track" hurricane database (HURDAT2; Landsea and Franklin 2013) for the North Atlantic and eastern North Pacific basins through the 2016 season. Similar files are provided by the Joint Typhoon Warning Center for the remainder of the TC basins. For this study, the TC location and 6-h motion vector along with the maximum wind speed are collocated in time with each scatterometer file. For reasons similar to using best-track data, vertical wind shear data are obtained from the Statistical Hurricane Intensity Prediction Scheme (SHIPS) database (DeMaria and Kaplan 1994, 1999) for the same periods as the best-track data. Shear is calculated for a deep layer (between 200 and 850 hPa), and the vortex has been removed 500 km radially outward of the TC center. Data are available for the entire study period for all basins with the exception of the first few storms of 2000 for the northwest Pacific basin. Vertical wind shear data are provided at 6-hourly intervals in the same manner as the best-track data. Discussion of the practicality of using a shallow shear layer is presented briefly in KJ16, where they determined the deep-layer shear is suitable for the purpose of the current study.

3. Methods for producing low-wavenumber analyses with scatterometer data

a. *Low-wavenumber analysis and compositing procedures*

To determine and quantify motion and shear-dependent, low-wavenumber asymmetric surface wind structure using global scatterometer data, this study expands on previous work from Vukicevic et al. (2014) and U14 that examined surface wind asymmetry from SFMR and model data. These studies describe a Fourier decomposition method for determining the low-wavenumber field written as

$$V(r,\theta) = V_0(r) + V_1\cos[\theta - \alpha_1(r)] + \varepsilon(r), \qquad (1)$$

where V_0 and V_1 are the wavenumber-0 and -1 amplitudes, respectively; α_1 is the wavenumber-1 phase; and ε is the total remaining contribution of the higher-order wavenumbers. This V is defined on a polar coordinate grid, where r and θ are the radial and azimuthal

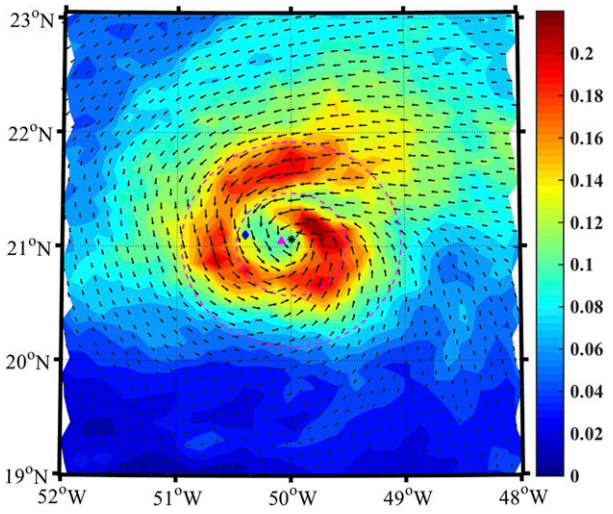

FIG. 2. Fore and aft (horizontal polarization) combined backscatter coefficient (dB, color shaded) and wind vectors are shown for Hurricane Isabel on 10 Sep 2003. The black asterisk within the backscatter weakness and circulation-defined center indicates the center position used in the subsequent low-wavenumber analysis. The magenta triangle and blue diamonds indicate the center positions based on the minimum in backscatter coefficient and best track, respectively.

coordinates, respectively. At the radius of maximum wind (RMW) and associated azimuth, Eq. (1) becomes the representative of $V_{\max}$ (TC intensity).

Low-wavenumber analyses for the scatterometer are processed in a similar fashion to the SFMR described in U14, with the exception that there is better azimuthal coverage. For this particular type of analysis, defining a center is critical. Unfortunately, the center cannot be defined strictly by the wind circulation because of the direction ambiguity issues previously described, but the backscatter coefficient (σ_0) can assist in determining a TC center. In many cases, especially hurricanes, there is a weakness in the σ_0 field near the center due to the presence of a precipitation-free eye. The center for the scatterometer analysis is subjectively defined by a combination of circulation, σ_0 (fore and aft horizontal polarization), and interpolated best-track position, with emphasis on the circulation and backscatter signatures. An example of the backscatter coefficient from Hurricane Isabel on 10 September 2003 is provided in Fig. 2. For this particular case, the circulation and σ_0 fields coincide well with each other, making it easier to determine the center. In weaker cases, such as tropical depressions, this is not so easily determined (see Fig. 12 in Stiles et al. 2014). In the instances when the minimum backscatter and circulation center are not well defined, the interpolated best-track center position is given the most consideration in the subjective center estimate. Often, this position lies between the minimum backscatter and wind circulation estimates and maintains a reasonable center depiction based on the available information.

Once a center is determined, the data are converted from an earth-relative Cartesian grid to a storm-centered polar coordinate grid. While the swath data maintain a 12.5-km resolution prior to conversion, the radial change in distance between points is not equidistant on the polar grid. Therefore, varying radii along each azimuth could pose a problem for obtaining a reasonable low-wavenumber analysis. During the grid conversion, radial errors are calculated, resulting in a mean absolute error of 2.5 km. Incorporating this variability in the radial designation allows for 5-km windows centered on the desired radius. For example, the lowest radial bin of 6.25 km includes converted radii between 3.75 and 8.75 km.

For a mature hurricane, the inner-core generally extends ~200 km from the storm center (i.e., Uhlhorn and Nolan 2012, U14). In this work, which includes weaker tropical storms and hurricanes, it is necessary to extend this distance by 50 km to ensure the processes associated with the inner core are captured for most storm sizes. In fact, Chavas et al. (2016) note that analysis beyond ~250–300 km is not meaningful for this type of study. Based on the definition for a TC inner core, the radial binning process extends to 250 km from the storm center with increments of 6.25 km. After standardizing the radial grid, the azimuthal components of these locations are then combined with the wind data in a similar form to Eq. (1). An unconstrained nonlinear optimization function that minimizes the error between the function-determined values and the wind speed observations is then used to determine the Fourier parameters for wavenumber 1 at each radial bin. The wavenumber amplitudes and phases (V_n and α_n, where n represents wavenumber beginning at 0) are then calculated using the following equations:

$$V_n = \sqrt{[s^2_{(n\times2)} + s^2_{(n\times2)+1}]}$$
$$\alpha_n = a\tan2[s_{(n\times2)+1}, s_{(n\times2)}]. \quad (2)$$

In Eq. (2), s_n is the parameter determined by the optimization function. For solving to wavenumber 1, $V_0 = s_1$, $V_1 = \sqrt{(s_2^2 + s_3^2)}$, and $\alpha_1 = a\tan2(s_3, s_2)$.

The above description references an earth-relative framework, where the motion of the storm has not been removed from the wind vectors. Based on simple vector geometry, it is well known that winds are generally higher on the right (left) side of the motion vector for the Northern (Southern) Hemisphere and

TABLE 1. Basic statistics including mean, median, minimum, maximum, and peak percentage of RMW for each examined TC basin. RMW and frequency of occurrence are listed for the peak value. Similar values are provided for RMW determined from SFMR flights over the North Atlantic (U14). Basin names are abbreviated and include NATL, EPCP, WPAC, and SHEM.

	NATL	EPCP	WPAC	SHEM	SFMR
Mean (km)	64.2	57.2	61.8	59.4	35.9
Median (km)	55.3	47.8	54.1	51.3	34.6
Min (km)	27.4	28.5	30.9	28.7	9.9
Max (km)	125.0	125.0	125.0	125.0	81.5
Peak frequency [km, (%)]	34.2 (21.7)	31.6 (32.1)	32.0 (27.3)	31.6 (29.8)	24.3 (24.8)

that storm motion tends to dominate most surface wind features (i.e., U14). This result was also verified for scatterometer winds in KJ16. By removing the storm translation contribution to the winds, the asymmetry related to other components, such as wind shear, is more easily assessable in a storm-relative framework. Following the analysis methods above, low-wavenumber analyses are producible using the wind vectors within various frameworks (i.e., storm or shear relative). For details of the cases used in this study, please consult Table S1 in the supplemental information for KJ16.

b. *Determination of a radius of maximum wind from scatterometer data*

As part of the analysis procedures, it is necessary to calculate an RMW with each scatterometer case. The most extensive examination of surface RMW in TCs is expressed with the SFMR cases used in U14, which estimate a mean surface RMW of ~25 km. The cases used in U14, however, were all mature hurricanes with well-defined circulation patterns. A more recent study by Chavas et al. (2015) examines a subset (31 cases) of surface wind radial profiles from scatterometer and H*WIND (Powell et al. 1998) data products and estimates a mean RMW on the order of 30–40 km.

For the scatterometer dataset here, all TC intensities are used, and weaker storms tend to have much larger RMW results as their circulations are more disorganized. Ueno and Bessho (2011) note that the resolution of their scatterometer data limits any observations within 50 km, and they bound their RMW between 50 and 150 km. Their average RMW is 99 km. Because the resolution of the data used in the present study is increased twofold from that of Ueno and Bessho (2011), it is possible to obtain a minimum RMW near 25 km. As this is a global study, it is important that all attainable storm sizes are included, with the exception of very large storms (RMW > 125 km). By providing an upper RMW bound, it ensures that all cases can be examined to at least 2 × RMW and that the inner core of the TC is provided.

Basin statistics regarding mean and standard deviation of RMW as well as other parameters in this dataset are described in KJ16. Table 1 shows detailed RMW statistics for each TC basin as determined by the scatterometer data. Figure 3 shows the difference in distribution of RMW for each TC basin. These probability density functions (PDFs) indicate that while there are some differences in size between each basin, the scatterometer determines a ~30–35-km RMW peak probability for all basins in agreement with Chavas et al. (2015). Interestingly, the shape of the curve of the North Atlantic scatterometer dataset is similarly shaped to that of the SFMR, which confirms that the RMWs from scatterometers differ mainly because of their coarser resolution.

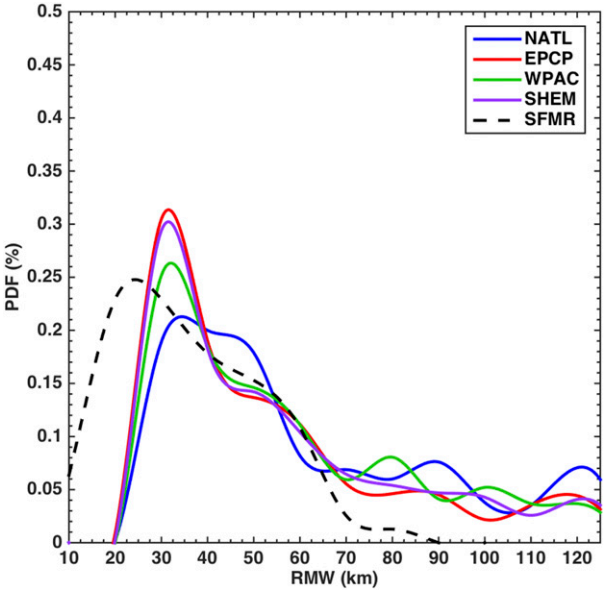

FIG. 3. PDFs of RMW for all cases with North Atlantic (NATL, blue), eastern and central North Pacific (EPCP, red), northwest Pacific (WPAC, green), and south Indian and southwest Pacific (SHEM, purple) curves are specifically represented. The PDFs of RMW determined from the SFMR data are also shown for North Atlantic cases (black).

TABLE 2. A compiled list of coincident SFMR and scatterometer cases is provided and separated based on TC intensity. In parentheses the SFMR offset in hours relative to the scatterometer time is shown. The flights in boldface were used in the comparison shown in Fig. 4.

Storm category	No. of cases	Storm names (year, SFMR offset)
TS	1	Katrina (2005, +2)
1	4	**Alex (2010, −1)**, **Igor (2010, −4)**, Karl (2010, +3), Rina (2011, −3)
2	3	Felix (2007, −2), **Danielle (2010, −4)**, Igor (2010, −4)
3	5	Bill (2009, −3), **Frances (2004, +3)**, Gustav (2008, −4), Ivan (2004, +4), Rina (2011, +5)
4	9	**Frances (2004, +4)**, **Danielle (2010, −4)**, **Earl (2010**, −1, 0, and **+1**), Ivan (2004, −2), Isabel (2003, +5), Rita (2005, +3 and +3)
5	2	**Ivan (2004, +5)**, **Katrina (2005, +5)**

c. *Compositing the low-wavenumber analyses*

Individual analyses of surface winds serve a variety of purposes for understanding storm-specific characteristics, but by creating composite analyses, it is much easier to determine prominent features within the surface field, including the asymmetric structure. The composite analyses are produced by averaging the individual fields on the normalized radial grid. Additionally, a weighting scheme based on the swath coverage percentage within 250 km of the TC center is used to ensure data quality and maximize the sample size. Effectively, 100% coverage within 125 km is required and >70% coverage is required through 250 km. The resulting weights are on a scale from 0 to 1, and only weights ≥ 0.7 are used. Because of this weighting scheme, KJ16 note that >75% of the cases have a weight of at least 0.9, so there is less likelihood of analysis problems as a result of a lack of coverage.

For this study, an emphasis is placed on TC intensity (Saffir–Simpson hurricane wind scale), storm motion, and vertical wind shear impacts on the surface wind asymmetry. Composites of these stratifications are computed for the full dataset. Because cases from the Southern Hemisphere are included, it is important to rotate these low-wavenumber analyses to a Northern Hemisphere frame of reference (as in Chen et al. 2006) in order to apply them correctly in the composite calculation. Further examination of motion and shear impacts is computed by comparing all shear conditions to low shear ($V_{\rm shr} < 3.2\,{\rm m\,s^{-1}}$), as well as the angle difference between the motion and shear vectors. The cutoffs for shear and motion are determined from the lower and upper 17.5% of the cumulative distribution function (CDF) of the respective variable, and they are comparable to those determined in Chen et al. (2006). Angle differences ($\Delta\theta_{\rm sm} = \theta_{\rm shr} - \theta_{\rm storm}$) also follow their methodology, where $|\Delta\theta_{\rm sm}| \leq 22.5°$ and $|\Delta\theta_{\rm sm}| \geq 157.5°$ are designated as the same and opposite, respectively. Angle differences for $22.5° < \Delta\theta_{\rm sm} < 157.5°$ and $-157.5° < \Delta\theta_{\rm sm} < -22.5°$ are designated as right and left, respectively.

4. Results and discussion

a. *Validation of the scatterometer analysis method using SFMR data*

The first goal of this study is to determine if the low-wavenumber analyses of scatterometer data resemble the analyses from SFMR. It has been established that the radial resolution of the scatterometer data is coarser than that of the SFMR, and this will ultimately affect the radial component of the analyses. Increased uncertainty in the scatterometer winds at higher wind speeds is indicative of increased differences between the maximum wavenumber-0 and -1 amplitude ($V_0 + V_1$) of the two wind sources. A statistical examination of a set of coincident cases is used to provide more substance to the results from KJ16. Table 2 provides a list of cases along with the scatterometer-relative offset time for SFMR. Of the 128 cases used in U14, 24 cases (~20%) overlapped, but only nine swaths met the 5-h offset and 70% coverage criteria. In Fig. 4a, maximum V_0 and V_1 for the scatterometer winds are plotted as a function of the coincident SFMR values. Note the shaded markers indicate the time offset in hours relative to the SFMR time. The text displayed in Fig. 4a is associated with weighted values of δV_0 and δV_1. The scatterometer maximum amplitudes compare well to the SFMR values as indicated by their correlation coefficients, but there is an expected tendency to underestimate the SFMR amplitude above $50\,{\rm m\,s^{-1}}$. Additionally, a weighted and paired Student's t test indicates that these results are statistically significant at 95%.

Figure 4b provides the scatter of α_1 at the maximum $V_0 + V_1$ for the scatterometer winds as a function of the associated SFMR α_1. Considering the time and resolution constraints, the wavenumber-1 phase agrees well with the coincident SFMR values, as indicated by the high correlation coefficient. One way to evaluate whether this is a reasonable difference between metrics is by following the methods in Lorsolo and Aksoy (2012). A root-mean-square maximum is calculated as a combination of a large amplitude or phase offset.

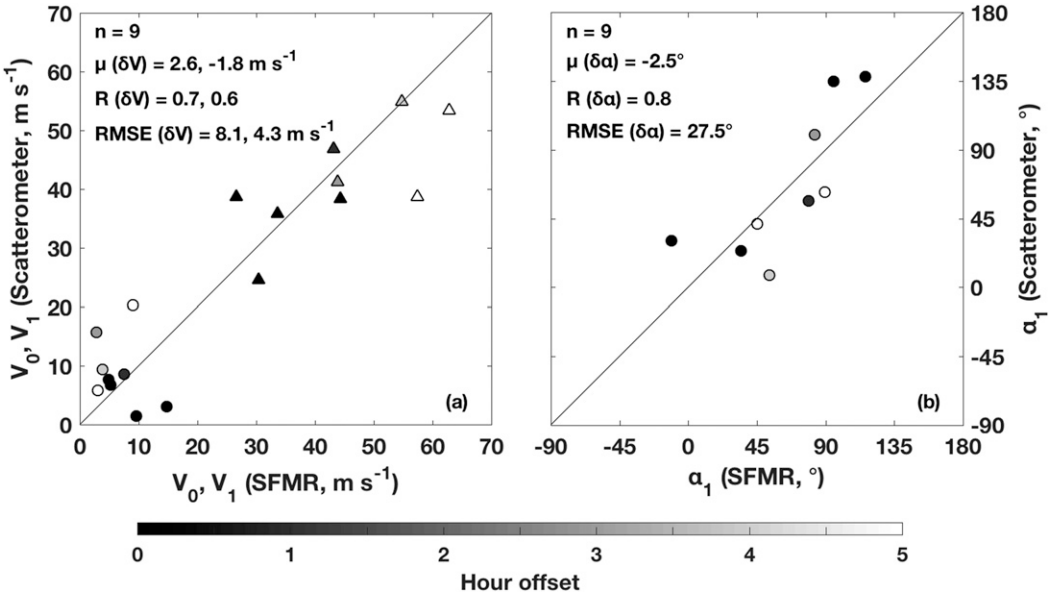

FIG. 4. (a) Maximum scatterometer wavenumber-0 and -1 amplitudes (V_0, triangles; V_1, circles) as a function of coincident (±5 h of scatterometer time) maximum SFMR amplitudes. Varying shades of gray of the markers indicate the SFMR hour offset. (b) The associated wavenumber-1 phases (α_1) at the maximum amplitudes are plotted in a similar manner to (a). Text values in each panel indicate weighted statistical values of the difference between the SFMR and scatterometer results, where the first set of values in (a) pertains to V_0.

Similar values for the difference between the SFMR and scatterometer wavenumber-1 signals are then produced. The resulting normalized RMS (variable *r* in their discussion) is 0.18. Assuming a 20% wavenumber-1 amplitude error, the phase error lies somewhere between 20° and 25°, which is similar to the weighted RMSE indicated in Fig. 4b. Despite the small sample, results for both amplitude and phase indicate that the scatterometer data are capable of providing reliable analyses and evaluation of the surface wind asymmetry.

b. Asymmetric structure as a function of TC intensity

The surface wind asymmetry is most clearly depicted as a dependence on storm intensity. The global composite analyses are displayed in Figs. 5a–c for tropical depressions and storms, category 1–2 (nonmajor) hurricanes, and category 3–5 (major) hurricanes, respectively. These composites are normalized based on the maximum amplitude of the composite (on a scale from 0 to 1) and are plotted on a normalized radial grid in a shear-direction-relative orientation (with storm motion removed). Note that the maximum low-wavenumber amplitude (black marker) tends to be located left of shear for tropical storms and nonmajor hurricanes while major hurricanes have their maxima located more downshear. For reference, shear-relative locations will be abbreviated as downshear (DS) or upshear (US) with left or right of the shear vector indicated by an L or an R, respectively. From a glance at the fields it is clear that the weaker systems have a more pronounced asymmetric structure overall. Note that these composites are statistically significant at 95% when compared to the overall global composite.

Going a step further, U14 examined the low-wavenumber amplitude and phase at the RMW with respect to storm motion and wind shear speed (see their Figs. 8 and 10). Their results indicate that increasing the storm motion is associated with an anticyclonic rotation of the phase from down-motion to right of motion while increasing the shear speed rotates the phase from downshear to left of shear. Note that for the motion-relative results, the motion vector has not been removed from the low-wavenumber analysis. Figure 6 provides a similar analysis but separated into TC intensity groups. In Fig. 6, the motion dependence is similar to that in U14, where α_1 rotates from down- to right of motion with increasing storm speed (V_{storm}). Nonmajor (major) hurricanes have the lowest (highest) correlation with increasing motion. It is generally assumed that an additional asymmetry of 90° to the right of motion should be applied to analyses of vortex structure, but Fig. 6 confirms U14's suggestion that this assumption is not always correct. Ueno and Kunii (2009) additionally suggest that the maximum wind (and effectively the low-wavenumber maximum) should occur 90° downwind of the maximum inflow. However, the parametric inflow

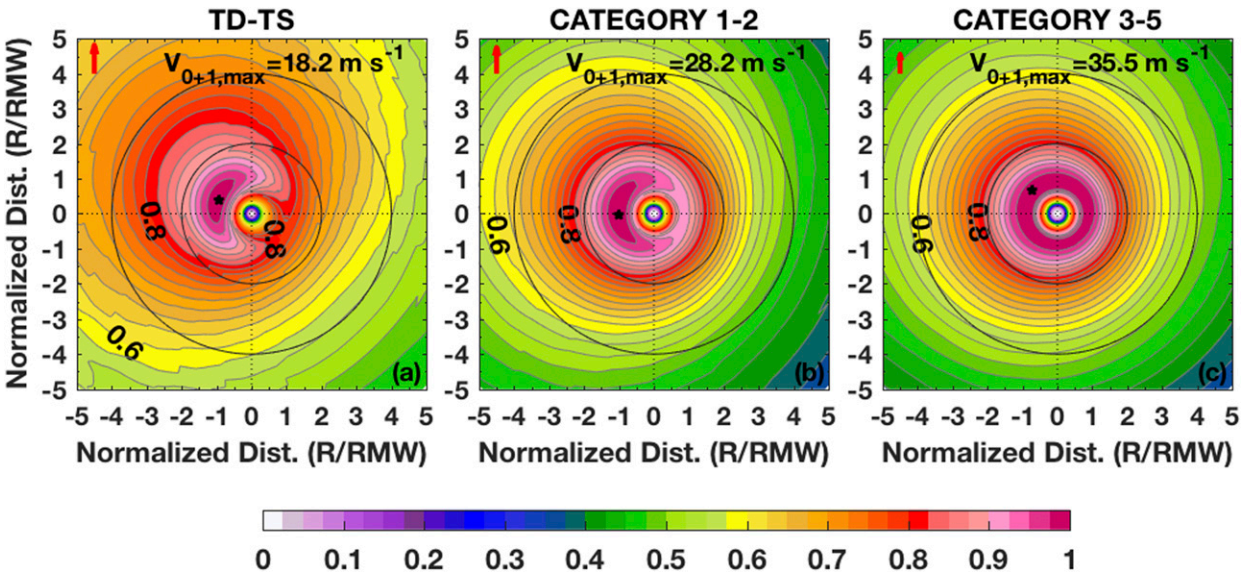

FIG. 5. Normalized composite shear-relative (with motion removed) wavenumber-0 and -1 two-dimensional scatterometer wind speed analyses as a function of normalized radius are provided for (a) tropical depressions and storms, (b) category 1 and 2 hurricanes, and (c) category 3–5 hurricanes. The red arrows (top of each panel) show the direction of shear and the black star marker indicates the location of the maximum amplitude. Contours and colors are plotted every 0.025 normalized units.

angle model described in Zhang and Uhlhorn (2012) indicates that the maximum inflow location near the RMW rotates cyclonically with increasing storm speed. Therefore, a cyclonic rotation of the low-wavenumber maximum would be expected. Based on the results presented here and in U14, the anticyclonic phase rotation is more a result of simple vector geometry where in slow-moving storms, the rotational component of the wind is controlled by internal vortex dynamics. Increasing the speed imparts an asymmetry on the winds that amplifies the maximum signal largely to the right of motion where the vectors align.

Figure 6b is similar to Fig. 6a in form but shows the change in wavenumber-1 phase at the RMW as a function of shear speed (V_{shr}) and within a shear-relative (storm motion removed) reference frame. For the tropical storm and nonmajor hurricane cases, α_1 rotates cyclonically from downshear to left of shear, which is

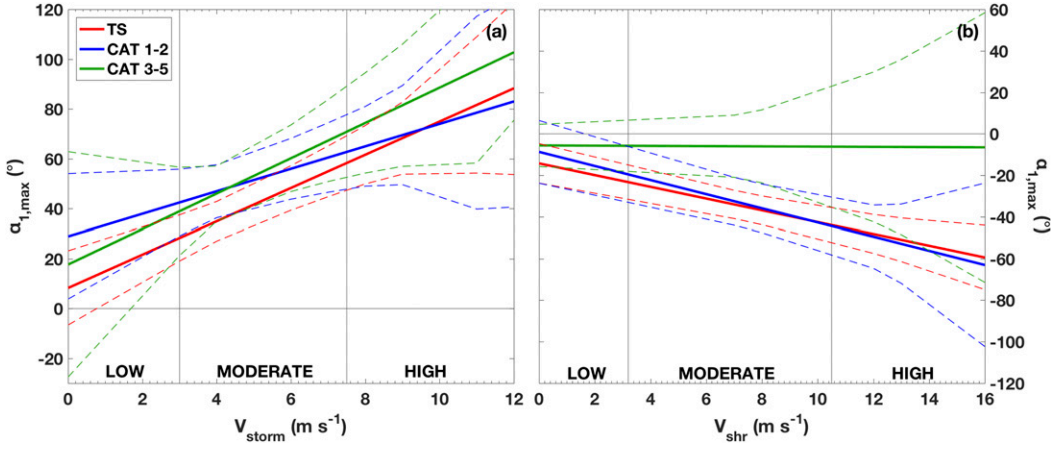

FIG. 6. (a) Linear regression fits of the wavenumber-1 phase at the maximum motion-relative amplitude ($\alpha_{1,max}$) are provided for three intensity groups—TS (red), category 1–2 (blue), and category 3–5 (green)—as a function of storm speed (V_{storm}). (b) As in (a), but in a shear-relative (motion removed) reference framework and as a function of vertical wind shear speed (V_{shr}). For reference, the zero line is indicative of the down-motion or down-shear direction, with negative phase angles representing locations to the left of motion or shear. Dashed lines indicate the 95% confidence interval of the respective fit.

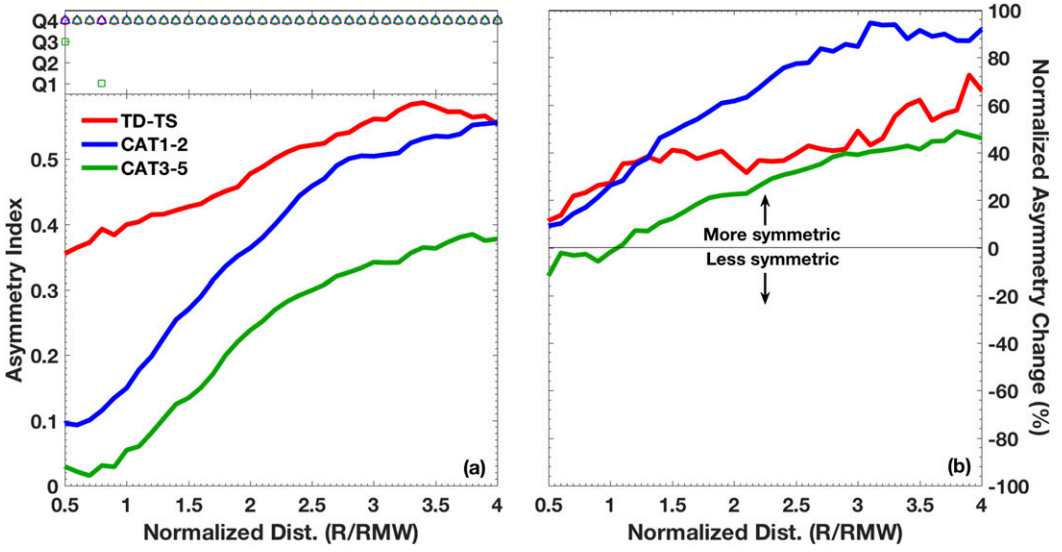

FIG. 7. (a) TC intensity-dependent radial profiles of wavenumber-1 asymmetry ratio (V_1/V_{0+1}) in the form of an asymmetry index (Alvey et al. 2015 ; Tao et al. 2017), where larger values indicate more asymmetry for: TS (red), category 1–2 (blue), and category 3–5 (green). The top inset in (a) indicates which of the four quadrant differences from Eq. (3) makes the largest contribution to the total asymmetry, and marker colors are as noted in the color legend. (b) The normalized percent change in asymmetry when evaluated against the asymmetry index for low wind shear cases ($V_{shr} < 3.2\ m\ s^{-1}$). Positive changes indicate that the structure becomes more symmetric relative to the full-shear composite.

similar to U14. However, the major hurricane cases have no observed correlation with increasing shear speed. This relationship could be a result of the scatterometer resolution and uncertainty at these high wind speeds. It is also possible that there is increased randomness to the location of the maximum amplitude in relation to shear, which could be explained by the principle of vortex resiliency (Reasor et al. 2004; Reasor and Eastin 2012). In this regard, the dynamics of the rotating vortex would maintain a symmetric system regardless of shear strength.

c. *Relative contribution of wind shear on TC surface wind structure*

Because Figs. 5 and 6 confirm results provided by U14 and KJ16, the necessary next step is to expand on this knowledge and to provide a detailed quantification of the surface wind asymmetry in response to wind shear. Using the two-dimensional composites of V_0 and V_1, ratios of wavenumber-1 amplitude to the total low-wavenumber amplitude (V_1/V_{0+1}) are calculated and mean radial profiles of this ratio are computed for each shear-relative quadrant. Following the description in Alvey et al. (2015) and Tao et al. (2017), a low-wavenumber asymmetry index (AIDX) is then determined from four absolute quadrant differences in the following manner:

$$\text{AIDX} = \sum_{i=1}^{4} Q_i \rightarrow \begin{cases} Q_1 = |\text{USR} - \text{DSR}| \\ Q_2 = |\text{USL} - \text{DSL}| \\ Q_3 = |\text{USL} - \text{DSR}| \\ Q_4 = |\text{DSL} - \text{USR}| \end{cases}. \quad (3)$$

Figure 7a shows radial profiles of AIDX as a function of TC intensity for the combined differences experiencing the full spectrum of wind shear. The tropical storm (TS) cases have the largest AIDX values at every normalized radius. It is clear to see that a majority of the contribution is coming from the absolute difference between the downshear-left and upshear-right quadrants as indicated by the markers in the inset panel. Both hurricane groups have successively lower asymmetry indices at all radii in these quadrants compared to the TS cases, but the gradient of AIDX is much larger between 1.0 and 2.5 × RMW. For comparison, AIDX within this radial range increases by ~1/3 of the RMW value for tropical storms while it nearly doubles to triples for nonmajor hurricanes. The change for major hurricanes follows a similar trend, but the difference is more pronounced, as AIDX is nearly 10 times larger at 2.5 × RMW than at the RMW. Near the RMW, the tropical storm cases are 3 times more asymmetric than the nonmajor hurricanes (and at least 15 times more asymmetric than major hurricanes). All differences in asymmetry described here are statistically significant at 95%.

These results indicate that tropical storms are generally asymmetric through most radii while hurricanes exhibit a larger symmetry in the inner region of the vortex before succumbing to other significant influences (shear, remaining motion impacts, or low-level local flow) with increasing radii.

By separating cases that experience low shear (452 cases), it is possible to compare with the results of a full range of shear and determine the relative impact of wind shear on the surface wind asymmetric structure. Figure 7b displays these radial profiles as the percentage change from the respective full shear profiles in Fig. 7a. Looking first at the region near the RMW, tropical storms and nonmajor hurricanes experience a 25% increase in symmetry, although the full shear asymmetry is low for the hurricane cases here. Major hurricanes show negligible change near the RMW due to shear. Outside the RMW, tropical storms are clearly impacted by shear, where AIDX is reduced by at least half at all radii. This reduction is more apparent in the nonmajor hurricanes with asymmetry ratios reduced in magnitude by upward of 60%–80% from the full shear profiles. Both hurricane groups are indicative of an asymmetric surface wind field that is highly dependent on wind shear outside the RMW. Asymmetry amplitudes could be increased upshear in weak systems if significant rain contamination remains in the dataset. Stiles et al. (2014) indicate that biases were eliminated in the problematic wind speed regimes. Therefore, any residual rain effects on the asymmetry of weak systems are likely insignificant.

One explanation for the lower asymmetry for nonmajor compared to major hurricanes goes back to the principles described by Fig. 6, where major hurricanes are more impacted by motion at storm speeds $> 5\,\mathrm{m\,s^{-1}}$. While Fig. 6 only shows the phase change, it stands to reason that residual motion impacts are larger for major hurricanes than nonmajor hurricanes, especially if the storms are moving faster. The PDF of storm speed as a function of nonmajor or major hurricane (not shown) indicates that major hurricanes have a 10%–15% greater chance of having speeds $> 5\,\mathrm{m\,s^{-1}}$. Conversely, nonmajor hurricanes have a ~10% greater probability of motion $< 5\,\mathrm{m\,s^{-1}}$. With slightly slower storm speeds combined with low shear, nonmajor hurricanes are 50% more symmetric than major hurricanes overall. However, it is clear that both hurricane groups are very symmetric within the low-shear constraints.

These asymmetry results assess the impact of wind shear on the surface wind structure, but it is important to consider their contribution relative to the total asymmetry. AIDX profiles are calculated from the full composite before motion removal as a function of TC intensity (not shown). Relative to the total asymmetry with full shear and motion included, the wind shear and residual factors contribute 62% and 47% near the RMW for tropical storms and nonmajor hurricanes, respectively. Motion accounts for 80% of the total asymmetry in major hurricanes. Outside the RMW, the wind shear (and residual) contribution to the total asymmetry is ~45%–55% regardless of intensity. These percentages indicate that wind shear has a similar or greater contribution to the total quantified surface wind asymmetry magnitude compared to motion in most circumstances. Of course, when the shear magnitude is reduced, the motion processes control the asymmetry magnitude, where the shear contribution is <20% at most radii and storm intensities.

d. Shear and motion angle difference and its influence on asymmetric structure

Another main question with regard to shear impacts is how does changing the shear direction in relation to motion affect the low-wavenumber surface wind speed asymmetry? U14 tried to diagnose this condition and found that the preference of left-of-shear asymmetry was prevalent in their four difference groups. A more detailed analysis of the impacts of shear's relation to motion is presented here by first showing the low-wavenumber field for each of the $\Delta\theta_{sm}$ groups in Fig. 8. These fields are presented identically to Fig. 5. All composites display a maximum wavenumber-0 + 1 field oriented on the left side of the shear, but clearly the change in θ_{sm} significantly (at 95%) impacts the amplitude and phase of the maximum.

The composite fields displayed indicate that the systematic preference for left-of-shear to downshear asymmetry as depicted in U14 may not always stand true. Because the scatterometer dataset contains tropical storms and the U14 dataset only includes hurricanes, it is possible that weak systems may be influenced more by the difference in the motion and shear. To determine if the strength of the system suggests a certain orientation, normalized bivariate PDFs of the wavenumber-1 phase at the maximum amplitude are plotted as a function of $\Delta\theta_{sm}$ in Fig. 9 for all storms (left panel) and for nonmajor hurricanes (right panel). Both joint PDFs indicate a statistically significant (95%) cyclonic rotation of the low-wavenumber asymmetric wind field if moving in order from left, same, right, to opposite. KJ16 noticed that after removing the motion vector, the maximum wind speed is oriented to the left of motion in tropical storms and nonmajor hurricanes. The same can be said for the low-wavenumber maxima as a function of $\Delta\theta_{sm}$, with the exception of the opposite group, compared to the median directions provided in Table 3. Note that the directional values in Table 3 are Earth relative.

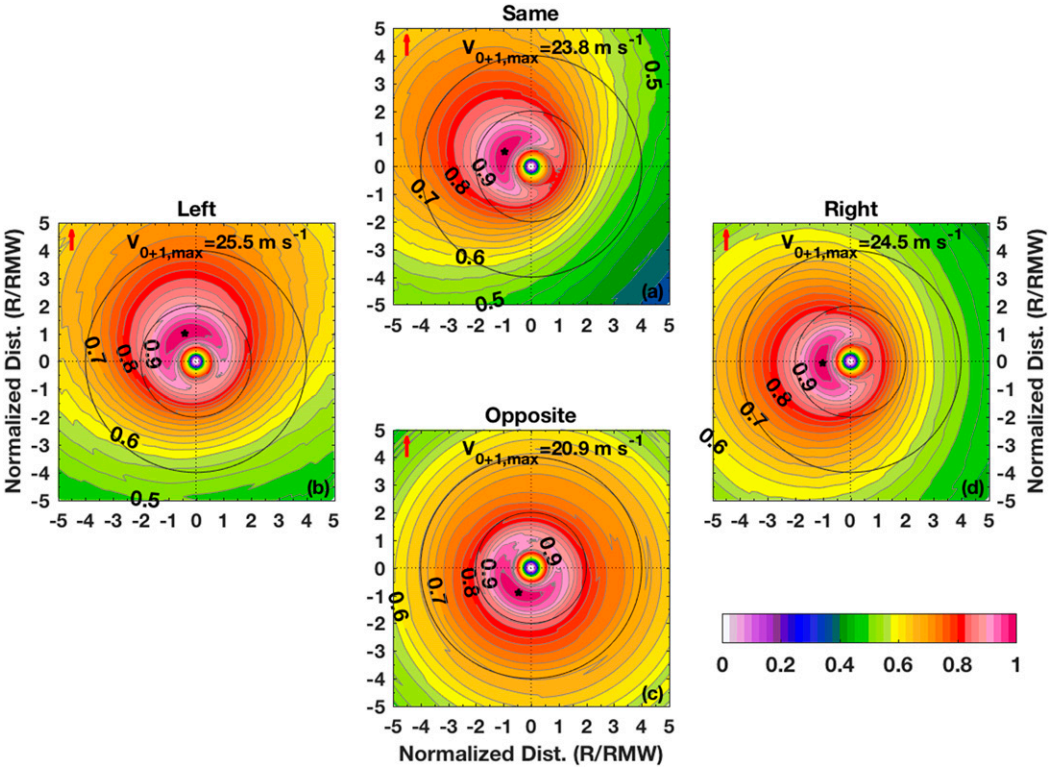

FIG. 8. Normalized composite analyses plotted similarly to Fig. 5 but for angle difference bins denoted as (a) same ($|\Delta\theta_{sm}| \leq 22.5°$), (b) left ($-157.5° < \Delta\theta_{sm} < -22.5°$), (c) opposite ($|\Delta\theta_{sm}| \geq 157.5°$), and (d) right ($22.5° < \Delta\theta_{sm} < 157.5°$).

Figure 10 shows the radial profiles of AIDX for the $\Delta\theta_{sm}$ groups similarly to Fig. 7. The largest asymmetry values for the full profiles, as well as near the RMW, are found when vectors point in the same direction while the lowest asymmetry values are found when vectors are oppositely directed. With the exception of the same compared to the left group (full shear), all profiles are significantly different at the 95% level. Note that the same and left groups are more asymmetric beyond the RMW (1.5–2.5 × RMW) compared to the tropical storm cases in Fig. 7. Considering that all groups have over 50% of their cases fitting the tropical storm classification and have similar median V_{storm} and V_{shr} (Table 3), it is evident that the differences in AIDX in Fig. 10 are a result of the angle differences themselves. After reducing the shear for the same group, the vortex is ~20%–25% more symmetric but remains highly asymmetric compared to the other groups. The opposite group becomes less symmetric beyond 2.5–3.0 × RMW after reducing shear. Also notice that the largest asymmetries occur in the difference between the upshear-left and downshear-right quadrants, which supports the upshear-left-oriented maximum in Fig. 9. In this instance, the presence of at least moderate shear seems to promote a more symmetric vortex as the low-shear conditions are ~15%–25% larger at all radii. Therefore, when vectors are oriented in the same direction or to the left of motion, the vortex will be highly asymmetric, whereas if they are oppositely oriented, a significantly more symmetric vortex is expected.

e. *Discussion*

KJ16 suggested the possibility that nonmajor hurricanes represent a transition stage between which shear and residual impacts both serve a prominent role in determining the asymmetric structure. Based on the AIDX profiles, this hypothesis seems justifiable near the RMW as the asymmetry induced by shear steadily decreases with increasing intensity (Fig. 7). However, this does not appear to hold true outside the RMW. If shear is the main contributor to asymmetry, reducing the shear should significantly reduce the wavenumber-1 asymmetry, which is generally what is portrayed in both hurricane groups. However, tropical storms exhibit a prominent asymmetric structure after reducing the shear. To help diagnose a possible explanation for the maintenance of the asymmetry, the difference in absolute angular momentum (AAM) flux between the

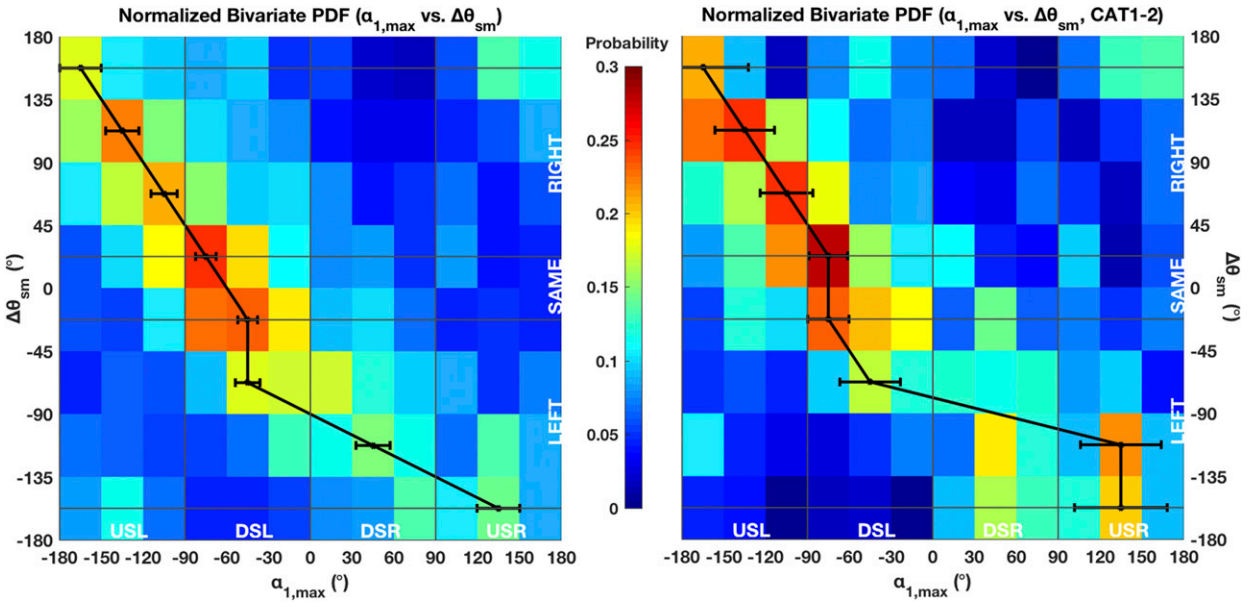

FIG. 9. (left) A normalized, bivariate PDF for all cases is provided as a function of wavenumber-1 phase ($\alpha_{1,\max}$) and of shear-motion angle differences ($\Delta\theta_{sm}$). (right) The same type of PDF but only is shown for category 1–2 hurricanes. The black line indicates the phase bin with the largest probability of occurrence with error bars indicating the 95% confidence intervals.

intensity groups should be revealing. A modified form of the initial AAM equation is given by Pálmen and Riehl (1957), but for the purposes of this study, quadrant-specific radial profiles of AAM flux (AAMF) are calculated using a modified version of Eq. (4) in Chan and Chan (2013), which takes the following form:

$$\mathrm{AAMF}(r) = r\overline{v}_\theta\overline{v}_r + r\overline{v'_\theta v'_r} + \frac{1}{2} fr^2\overline{v}_r + \frac{1}{2}r^2\overline{fv'_r} + F. \qquad (4)$$

Each quadrant is defined in the shear-relative range from $[-\pi, \pi]$ with increments of $\pi/2$ radians and where r is defined across the range of 0–250 km with 6-km radial increments. The frictional term[1] (F) is needed for momentum conservation purposes but has increased uncertainty within stronger wind speeds due to the constraints described in Powell et al. (2003). Terms with overbars represent quadrant averages and those with primes represent perturbations from the quadrant mean. The first two terms on the right side are referred to as the symmetric and asymmetric relative AAMF (i.e., SRAM and ARAM flux), respectively. Terms three and four on the right side represent the symmetric and asymmetric Coriolis torque (SCT and ACT, respectively). Holland (1983a) provides a detailed examination of the contribution of these terms and their influence on the TC structure. He describes that symmetric and asymmetric relative angular momentum act to import momentum toward the TC center, counteracted by frictional dissipation and an anticyclonic acceleration of momentum with increasing radius imparted by the symmetric torque term. Asymmetric torque is noted to only influence the circulation well away from the TC center; thus, it will not be discussed in this present study. The variable names used will follow those in Chan and Chan (2013), but within the quadrant-based framework, they are not truly symmetric or asymmetric as originally described as a result of the fact they do not refer to an entire 360° field. The purpose of separating AAMF into quadrants is to examine changes in relation to the wavenumber-1 asymmetry.

Because the AAMF is highly dependent on the tangential and radial winds, it is important to show the quality of these data from the scatterometer. Figure 11 shows shear-relative quadrant profiles of both wind

TABLE 3. Median values for motion and wind shear speed, direction, and direction difference are provided for each $\Delta\theta_{sm}$ group. Error estimates indicate 95% confidence intervals.

	V_{storm} (m s^{-1})	V_{shr} (m s^{-1})	θ_{storm} (°)	θ_{shr} (°)	$\Delta\theta_{sm}$ (°)
Same	5.0 ± 0.5	6.6 ± 0.4	−51 ± 6	−48 ± 7	0 ± 1
Left	4.0 ± 0.3	6.0 ± 0.3	−58 ± 4	−100 ± 7	−73 ± 3
Opposite	4.0 ± 0.5	6.1 ± 0.7	−62 ± 8	97 ± 13	160 ± 22
Right	5.0 ± 0.3	6.3 ± −0.3	−44 ± 4	47 ± 4	78 ± 2

[1] Here, $F = rC_D|v_s^2|$, where C_D is the drag coefficient (Powell 1980; Powell et al. 2003) and $|v_s|$ is the total surface wind speed.

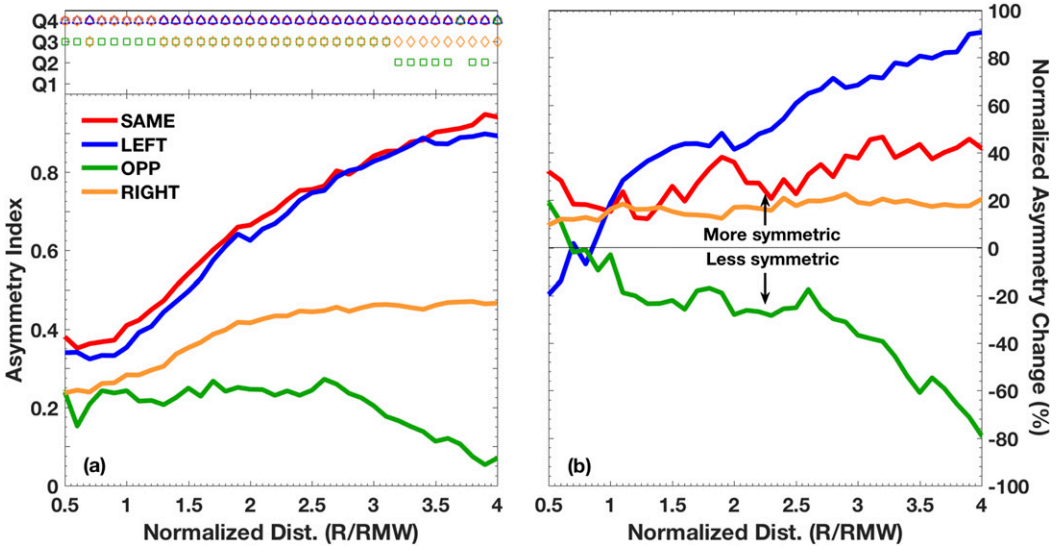

FIG. 10. As in Fig. 7, but for the $\Delta\theta_{sm}$ groups.

speeds as a function of TC intensity. Tangential (radial) wind peaks in the left-of-shear (downshear) quadrants, which agrees with the boundary layer results of Zhang et al. (2013). Therefore, these wind components are valid for evaluating AAMF. Quadrant profiles of near-surface AAMF are shown in Fig. 12 within a shear-relative reference frame. The tropical storm group does not have a strong peak in AAMF in any quadrant. The

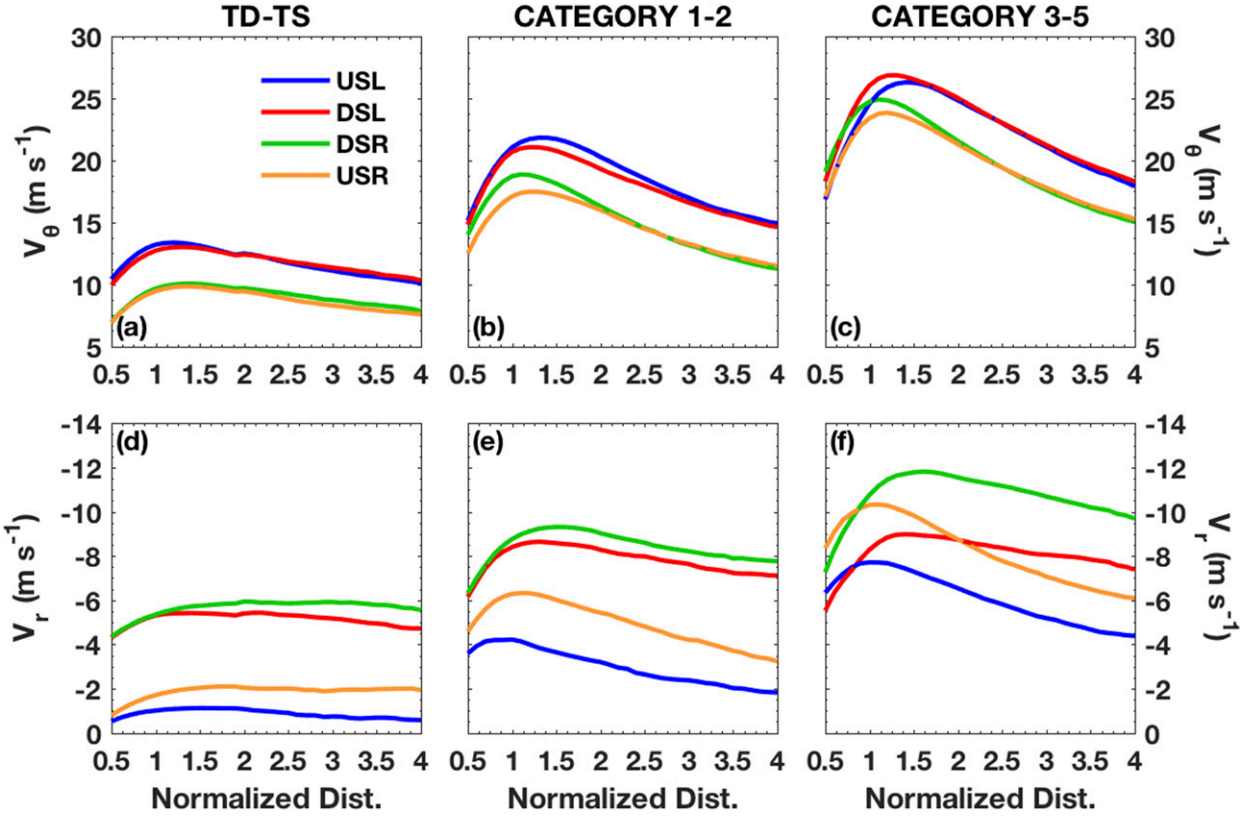

FIG. 11. Radial profiles of (a)–(c) tangential (v_θ) and (d)–(f) radial (v_r) wind speeds for (left to right) each storm intensity group as a function of shear-relative quadrant: USL (blue), DSL (red), DSR (green), and USR (orange).

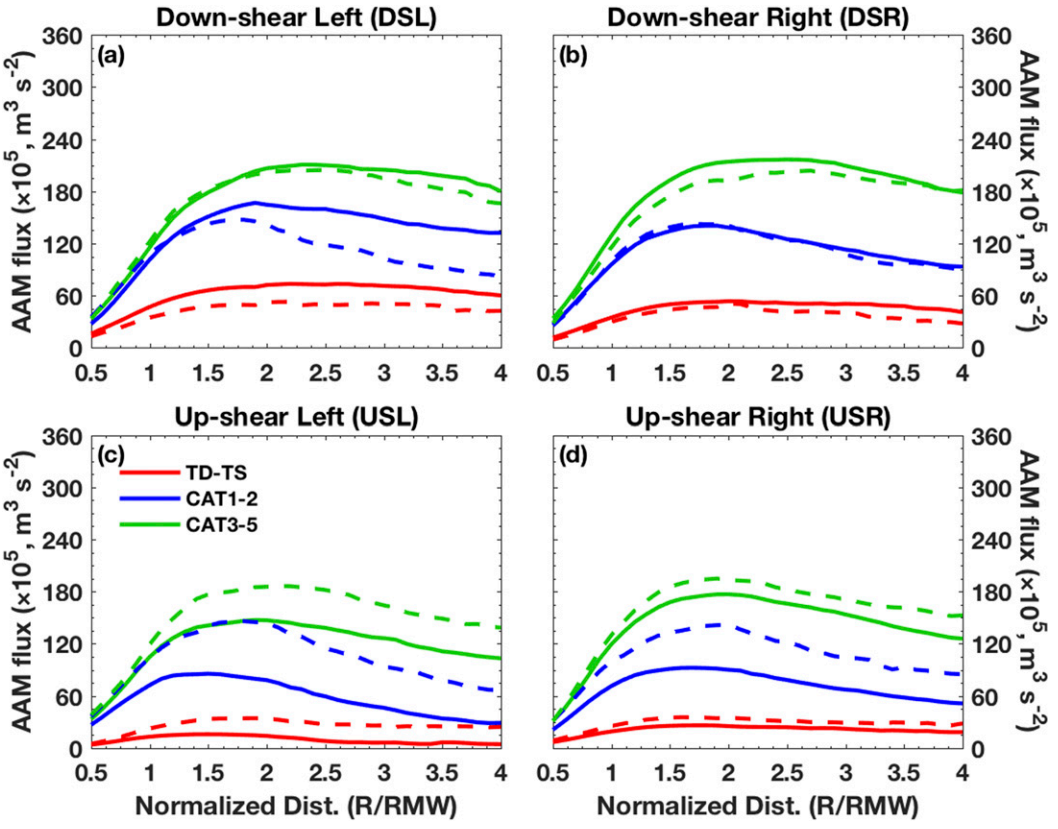

FIG. 12. Shear-relative quadrant profiles of surface absolute angular momentum flux ($\times 10^5$ m^3 s^{-2}) as a function of TC intensity—TD–TS (red), category 1–2 (blue), and category 3–5 (green)—for the full range of shear values (solid lines) and for low-shear conditions (dashed lines).

flux is higher in the downshear quadrants compared to the upshear quadrants, especially between 1.5 and 2.5 × RMW. Reducing the shear also lowers the magnitude of the AAMF downshear but increases the impact in the upshear quadrants. Shear in this instance induces an asymmetry, although weak, in the AAM transport that is maximized downshear. For the nonmajor (major) hurricane group, a larger amount of AAMF occurs between 1.5 and 2.5 × RMW in the downshear-left (downshear right) quadrant compared to the other three quadrants. This large momentum flux extends consistently beyond 3 × RMW, but at lower values of shear, the AAMF asymmetry is significantly decreased upshear in this region.

The quadrant containing the maximum AAMF has a combination of large v_θ and v_r, as Eq. (4) and Fig. 11 suggest, but the individual components of Eq. (4) reveal the relative contributions of each to the total AAMF. Table 4 provides the intensity-dependent percentages for each term (except the asymmetric torque term) at 0.5, 1, 2, and 3 × RMW for the quadrant with the largest AAMF in Fig. 12. Percentages are given relative to the total

TABLE 4. Percent contributions of the individual absolute angular momentum flux terms in Eq. (4) (excluding the asymmetric torque term) are provided as a function of TC intensity, where the left, middle, and right values (separated by commas) indicate the results for tropical storms, nonmajor hurricanes, and major hurricanes, respectively. The percentages are shown relative to the total AAMF and when combined will equal 100%. The values are only provided for the quadrant with the largest angular momentum flux as shown in Fig. 12.

	SRAM (%)	ARAM (%)	SCT (%)	F (%)
0.5 × RMW	128.6, 126.0, 128.4	6.3, 7.3, 7.1	−11.8, −7.9, −3.8	−23.1, −25.4, −31.8
1 × RMW	131.5, 121.4, 114.1	6.4, 4.4, 7.9	−20.1, −11.5, −6.2	−17.8, −14.4, −14.8
2 × RMW	155.5, 133.4, 122.7	7.7, 6.3, 5.2	−45.4, −26.4, −16.8	−17.7, −13.3, −10.9
3 × RMW	168.4, 146.6, 137.4	9.7, 7.5, 5.3	−59.4, −39.5, −31.1	−18.7, −14.6, −11.3

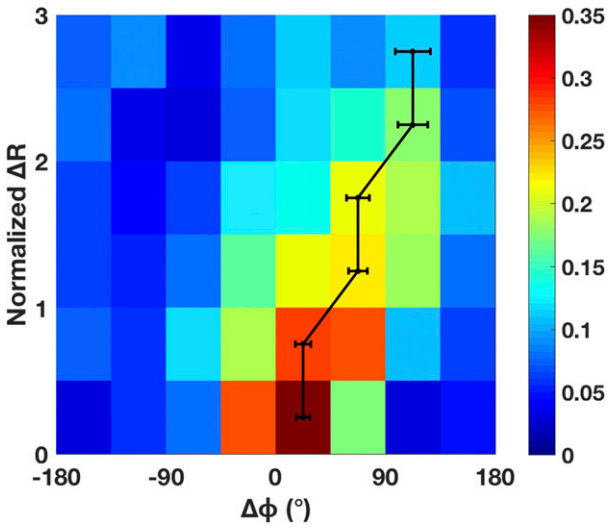

FIG. 13. Similar to Fig. 9, a joint PDF of the azimuthal difference ($\Delta\phi = \phi_{\text{aamf}} - \alpha_{1,\max}$) and normalized radial difference (ΔR) of the maximum AAMF and the peak wavenumber-1 asymmetry is provided. Positive $\Delta\phi$ values indicate an upwind rotation of the AAMF relative to the wavenumber-1 peak.

AAMF at a particular radius. Because the symmetric flux term is larger than the total AAMF, which includes the inhibiting forces of friction and Coriolis torque, the symmetric flux value exceeds 100%. Therefore, when all percentages for a particular intensity and radius are combined, the value will equal 100%. The symmetric flux is clearly the dominant term, which increases at larger radii due to wind shear influences on the vortex outside the RMW. The asymmetric flux follows similar trends with downshear maxima present, but the relative contribution of this term is ~6%–10% near the peak AAMF at ~2 × RMW. Outside 2 × RMW, the symmetric torque term begins to more significantly influence the symmetric momentum import. Friction also has a large impact on the momentum transport, especially at or within the RMW where it reduces the transport by 25%–30%. Cases experiencing moderate-to-strong shear are able to somewhat resist these opposing forces, but lowering the shear (not shown) dampens this increased inward momentum transport and allows the symmetric flux to have greater influence on the vortex as a whole. The presence of shear amplifies the AAM flux downshear in all intensity groups and generally increases the inward AAM transport upwind of the region of maximum low-wavenumber surface wind speed asymmetry.

To quantify this statement, a normalized bivariate PDF of the azimuthal and radial offset of the maximum AAMF relative to the maximum wavenumber-1 surface wind speed asymmetry is provided in Fig. 13 for tropical storms and nonmajor hurricanes. The azimuthal change is identified as $\Delta\phi = \phi_{\text{aamf}} - \alpha_{1,\max}$, where a positive value indicates an upwind rotation relative to the low-wavenumber wind speed maximum. If the peak AAMF occurs radially close to the maximum low-wavenumber amplitude, the AAMF is likely to occur in tandem with the peak wind speed asymmetry. In the scenario showcased in Fig. 12 where the peak AAMF occurs between 1.5 and 2.5 × RMW, the azimuthal offset is likely to occur 45°–90° upwind of the maximum asymmetry amplitude. This relationship is a reflection of a sheared surface wind structure because low-shear cases (not shown) do not exhibit such a strong signal in the azimuthal offset. It is also prevalent for the θ_{sm} groups (not shown) and indicates that increased AAMF downshear left or left of shear for an oppositely pointing shear and motion vector would produce the observed upshear-left asymmetry.

The AAMF profiles shown complement a recent study by Zhang et al. (2013) that examined the shear-relative boundary layer structure in hurricanes based on a large GPS dropsonde database. They found that low-level (100–150 m) inflow maximizes downshear right between 1.5 and 2.0 × RMW and strong inflow extends beyond 3 × RMW. They also found a statistically significant difference in 50-m specific humidity when comparing downshear-right and upshear-left quadrants. The moister downshear-right low-level conditions are out of phase with radar data collected at 1.5-km altitude (i.e., top of the boundary layer), which by speculation might suggest that the downshear-right region acts as a source location for potential buildup of convection. Hence and Houze (2011) noted that convective updrafts tend to be triggered in the downshear-right eyewall region during strong hurricanes, providing more supporting evidence for this possible downshear-right development region.

Didlake and Houze (2013) also describe in a case study of Hurricane Rita (2005) that stratiform rainband dynamics could conceivably have impacts on boundary layer or surface level processes. These authors found increased inflow at ~2–2.5 × RMW at ~1-km altitude in conjunction with increased updraft speeds. They also describe the formation of a 3-km-altitude wind speed jet that maximizes upshear left, potentially mixing outflow into the boundary layer and reducing the AAMF upshear. Considering that AAM transport is maximized downshear to downshear right in the range of 1.5–2.5 × RMW and overlaps a region of increased surface convergence, moisture, and inflow, one possible connection is that increased AAMF could help promote a region of developing convection that ultimately rotates cyclonically and matures in the downshear-left quadrant. Additionally, the downshear to downshear-right AAMF maximum could be tied to low-level environmental flow (Reasor et al. 2013) that is associated with the formation

of the downshear-left precipitation maximum in sheared TCs. Looking back at the location of the maximum low-wavenumber asymmetry (Fig. 5), the maximum asymmetric surface wind structure forms downwind of the maximum AAMF and associated convective and thermodynamic components, potentially as a result of rather than a cause of their development.

One complication is that a locally induced shear or imposing flow at low levels is not considered in the analyses. Reasor et al. (2013) stipulates that the local storm-induced wind shear is generally to the right of the environmental shear, producing a low-level flow across the vortex from downshear right to downshear left. These authors also show that the maximum vertical velocity is oriented downshear (with some variability in the downshear-right direction), which supports a convective maximum downwind (or downshear left) similarly to other convective asymmetry studies (Chen et al. 2006; Wingo and Cecil 2010; Hence and Houze 2011; Jiang et al. 2013; Zagrodnik and Jiang 2014; Tao and Jiang 2015). This convective asymmetry is likely going to have an influence on the surface wind structure as well (U14; Ueno and Kunii 2009) but generally developing a left-of-shear to downshear-left maximum wind asymmetry. While not verified in this present study, it is possible to consider that only for oppositely pointing shear and motion vectors, the superimposed low-level flow along with the convective maximum pose an alternative setup compared to the result of Reasor et al. (2013) from above, where a convective maximum occurs more to the left of the environment shear value. This in turn would imply that increased angular momentum transport should occur downshear left and promote a wind speed asymmetry upshear left. The processes involved clearly necessitate more investigation.

5. Summary and conclusions

In this study, a large dataset of scatterometer surface winds is utilized to determine detailed information about the low-wavenumber asymmetric surface wind structure and to quantify the vertical wind shear influence on this structure. Several previous studies using aircraft data (Rogers and Uhlhorn 2008; U14) and satellite data (Ueno and Kunii 2009; Ueno and Bessho 2011) provide insight into the expected relationships between wind shear and storm motion and their relative impact on the surface wind asymmetry. However, these studies are limited in terms of the scope of their dataset or which types of TCs are included in their analyses. While inherent with several drawbacks, the global scatterometer dataset provides an avenue for obtaining statistically sound results for various stratifications within the low-wavenumber, Fourier decomposition framework discussed in U14 and Vukicevic et al. (2014).

At the beginning of this study, we sought to answer several important questions regarding the applicability of the data and methods used as well as diagnosing and quantifying the general structure and asymmetry of surface wind speed in the presence of shear. Based on the results of the composite analyses and discussion of mechanisms for the various differences in the low-wavenumber asymmetry, the following main conclusions provide answers to those questions:

- Corrected scatterometer winds in association with the described analysis method are generally representative and useful for diagnosing low-wavenumber asymmetric surface wind structure in TCs after evaluating against a small yet trustworthy subsample of the SFMR dataset in Uhlhorn et al. (2014).
- Examination of the asymmetry index compared to cases that experience weak wind shear reveals that tropical storms are the most asymmetric of the TC intensity groups near the RMW but that all intensity groups are statistically significantly impacted by shear outside the RMW.
- When changing the shear heading in relation to motion from left, same, right, or opposite, the maximum asymmetry (near the RMW) rotates cyclonically from DS, DSL, LS, to USL, respectively. The order of these groups is also the general order of the magnitude of their asymmetry, where the same and left groups (opposite) are highly asymmetric (symmetric) in the presence of shear.
- Absolute angular momentum flux profiles in the presence of shear suggest that an infusion of larger momentum occurs downshear such that an increase of inward momentum flux is found upwind of the surface wind asymmetry maximum.

The idea of importation or increase in the inward transport of absolute angular momentum upwind of the low-wavenumber maximum suggests a coincident occurrence with the development of upward motion (Ueno and Kunii 2009; Hence and Houze 2011; Reasor et al. 2013) as well as a possible influence from rainband dynamics (Didlake and Houze 2013). The momentum mechanism appears to be a robust and important connection between the precipitation and thermodynamic structure and suggests that the prominent surface wind asymmetry is potentially an effect of rather than a cause of such processes. A forthcoming companion study (Part II, Klotz and Jiang 2017, manuscript submitted to *Mon. Wea. Rev.*) related to this work will discuss the change in surface wind structure as it pertains to intensity change events.

Acknowledgments. Support for this study was provided by NASA New Investigator Program (NIP) Award NNX10AG55G and NASA Hurricane Science Research Program (HSRP) Grant NNX10AG34G under the direction of Ramesh Kakar. The scatterometer data were provided by NASA JPL through their TCIS archive (tropicalcyclone.jpl.nasa.gov or ftp://mwsci.jpl.nasa.gov/). NOAA's Aircraft Operations Center and Hurricane Research Division collected and provided the quality-controlled aircraft data, respectively. Comments from internal reviewers at the Hurricane Research Division as well as helpful reviews by several external colleagues significantly aided the quality of this presented work.

REFERENCES

Aberson, S. D., M. L. Black, R. A. Black, J. J. Cione, C. W. Landsea, F. D. Marks, and R. W. Burpee, 2006: Thirty years of tropical cyclone research with the NOAA P-3 aircraft. *Bull. Amer. Meteor. Soc.*, **87**, 1039–1055, doi:10.1175/BAMS-87-8-1039.

Alvey, G., III, J. Zawislak, and E. J. Zipser, 2015: Precipitation properties observed during tropical cyclone intensity change. *Mon. Wea. Rev.*, **143**, 4476–4492, doi:10.1175/MWR-D-15-0065.1.

Bessho, K., M. DeMaria, and J. A. Knaff, 2006: Tropical cyclone wind retrievals from the Advanced Microwave Sounder Unit (AMSU): Application to surface wind analysis. *J. Appl. Meteor. Climatol.*, **45**, 399–415, doi:10.1175/JAM2352.1.

Black, M. L., R. W. Burpee, and F. D. Marks Jr., 1997: The asymmetric distribution of vertical motions and precipitation in the hurricane eyewall. Preprints, *22nd Conf. on Hurricanes and Tropical Meteorology*, Fort Collins, CO, Amer. Meteor. Soc., 100–101.

Brand, S., C. A. Buenafe, and H. D. Hamilton, 1981: Comparison of tropical cyclone motion and environmental steering. *Mon. Wea. Rev.*, **109**, 908–909, doi:10.1175/1520-0493(1981)109<0908:COTCMA>2.0.CO;2.

Brennan, M. J., C. C. Hennon, and R. D. Knabb, 2009: The operational use of QuikSCAT ocean surface vector winds at the National Hurricane Center. *Wea. Forecasting*, **24**, 621–645, doi:10.1175/2008WAF2222188.1.

Burpee, R. W., and M. L. Black, 1989: Temporal and spatial variations of rainfall near the centers of two tropical cyclones. *Mon. Wea. Rev.*, **117**, 2204–2218, doi:10.1175/1520-0493(1989)117<2204:TASVOR>2.0.CO;2.

Chan, J. C.-L., and R. T. Williams, 1987: Analytical and numerical studies of the beta-effect in tropical cyclone motion. Part I: Zero mean flow. *J. Atmos. Sci.*, **44**, 1257–1265, doi:10.1175/1520-0469(1987)044<1257:AANSOT>2.0.CO;2.

Chan, K. T.-F., and J. C.-L. Chan, 2013: Angular momentum transports and synoptic flow patterns associated with tropical cyclone size change. *Mon. Wea. Rev.*, **141**, 3985–4007, doi:10.1175/MWR-D-12-00204.1.

Chavas, D. R., N. Lin, and K. Emanuel, 2015: A model for the complete radial structure of the tropical cyclone wind field. Part I: Comparison with observed structure. *J. Atmos. Sci.*, **72**, 3647–3662, doi:10.1175/JAS-D-15-0014.1.

——, ——, W. Dong, and Y. Lin, 2016: Observed tropical cyclone size revisited. *J. Climate*, **29**, 2923–2939, doi:10.1175/JCLI-D-15-0731.1.

Chen, S. S., J. A. Knaff, and F. D. Marks Jr., 2006: Effects of vertical wind shear and storm motion on tropical cyclone rainfall asymmetries deduced from TRMM. *Mon. Wea. Rev.*, **134**, 3190–3208, doi:10.1175/MWR3245.1.

Corbosiero, K. L., and J. Molinari, 2003: The relationship between storm motion, vertical wind shear, and convective asymmetries in tropical cyclones. *J. Atmos. Sci.*, **60**, 366–376, doi:10.1175/1520-0469(2003)060<0366:TRBSMV>2.0.CO;2.

DeMaria, M., and J. Kaplan, 1994: A Statistical Hurricane Intensity Prediction Scheme (SHIPS) for the Atlantic basin. *Wea. Forecasting*, **9**, 209–220, doi:10.1175/1520-0434(1994)009<0209:ASHIPS>2.0.CO;2.

——, and ——, 1999: An updated Statistical Hurricane Intensity Prediction Scheme (SHIPS) for the Atlantic and eastern North Pacific basins. *Wea. Forecasting*, **14**, 326–337, doi:10.1175/1520-0434(1999)014<0326:AUSHIP>2.0.CO;2.

Demuth, J., M. DeMaria, J. A. Knaff, and T. H. Vonder Haar, 2004: Validation of an Advanced Microwave Sounder Unit (AMSU) tropical cyclone intensity and size estimation algorithm. *J. Appl. Meteor.*, **43**, 282–296, doi:10.1175/1520-0450(2004)043<0282:EOAMSU>2.0.CO;2.

——, ——, and ——, 2006: Improvement of Advanced Microwave Sounding Unit tropical cyclone intensity and size estimation algorithms. *J. Appl. Meteor. Climatol.*, **45**, 1573–1581, doi:10.1175/JAM2429.1.

Didlake, A. C., and R. A. Houze Jr., 2013: Dynamics of the stratiform sector of a tropical cyclone rainband. *J. Atmos. Sci.*, **70**, 1891–1911, doi:10.1175/JAS-D-12-0245.1.

Draper, D. W., and D. G. Long, 2002: An assessment of SeaWinds on QuikSCAT wind retrieval. *J. Geophys. Res.*, **107**, 3212, doi:10.1029/2002JC001330.

——, and ——, 2004: Simultaneous wind and rain retrieval using SeaWinds data. *IEEE Trans. Geosci. Remote Sens.*, **42**, 1411–1423, doi:10.1109/TGRS.2004.830169.

Dvorak, V. F., 1975: Tropical cyclone intensity analysis and forecasting from satellite imagery. *Mon. Wea. Rev.*, **103**, 420–430, doi:10.1175/1520-0493(1975)103<0420:TCIAAF>2.0.CO;2.

Figa-Saldaña, J., J. J. W. Wilson, E. Attema, R. Gelsthorpe, M. R. Drinkwater, and A. Stoffelen, 2002: The Advanced Scatterometer (ASCAT) on the Meteorological Operational (MetOp) platform: A follow on for European wind scatterometers. *Can. J. Remote Sens.*, **28**, 404–412, doi:10.5589/m02-035.

Fiorino, M., and R. L. Elsberry, 1989: Contributions to tropical cyclone motion by small, medium and large scales in the initial vortex. *Mon. Wea. Rev.*, **117**, 721–727, doi:10.1175/1520-0493(1989)117<0721:CTTCMB>2.0.CO;2.

Frank, W. M., and E. A. Ritchie, 1999: Effects of environmental flow upon tropical cyclone structure. *Mon. Wea. Rev.*, **127**, 2044–2061, doi:10.1175/1520-0493(1999)127<2044:EOEFUT>2.0.CO;2.

Franklin, J. L., S. J. Ford, S. E. Feuer, and F. D. Marks Jr., 1993: The kinematic structure of Hurricane Gloria (1985) determined from nested analyses of dropwindsonde and Doppler radar data. *Mon. Wea. Rev.*, **121**, 2433–2451, doi:10.1175/1520-0493(1993)121<2433:TKSOHG>2.0.CO;2.

——, M. L. Black, and K. Valde, 2003: GPS dropwindsonde wind profiles in hurricanes and their operational implications. *Wea. Forecasting*, **18**, 32–44, doi:10.1175/1520-0434(2003)018<0032:GDWPIH>2.0.CO;2.

George, J. E., and W. M. Gray, 1976: Tropical cyclone motion and surrounding parameter relationships. *J. Appl. Meteor.*, **15**, 1252–1264, doi:10.1175/1520-0450(1976)015<1252:TCMASP>2.0.CO;2.

Gonzalez, I., III, A. Cotto, and H. E. Willoughby, 2015: Synthesis of vortex Rossby waves. Part II: Vortex motion and waves in the outer waveguide. *J. Atmos. Sci.*, **72**, 3958–3974, doi:10.1175/JAS-D-15-0005.1.

Goodberlet, M. A., C. T. Swift, and J. C. Wilkerson, 1989: Remote sensing of ocean surface winds with the Special Sensor Microwave/Imager. *J. Geophys. Res.*, **94**, 14 547–14 555, doi:10.1029/JC094iC10p14547.

Gray, W. M., 1968: Global view of the origin of tropical disturbances and storms. *Mon. Wea. Rev.*, **96**, 669–700, doi:10.1175/1520-0493(1968)096<0669:GVOTOO>2.0.CO;2.

——, 1979: Hurricanes: Their formation, structure, and likely role in tropical circulation. *Meteorology over the Tropical Oceans*, D. B. Shaw, Ed., Royal Meteorological Society, 155–218.

Hence, D. A., and R. A. Houze Jr., 2011: Vertical structure of hurricane eyewalls as seen by the TRMM Precipitation Radar. *J. Atmos. Sci.*, **68**, 1637–1652, doi:10.1175/2011JAS3578.1.

Hendricks, E. A., M. S. Peng, B. Fu, and T. Li, 2010: Quantifying environmental control on tropical cyclone intensity change. *Mon. Wea. Rev.*, **138**, 3243–3271, doi:10.1175/2010MWR3185.1.

Hock, T. F., and J. L. Franklin, 1999: The NCAR GPS dropwindsonde. *Bull. Amer. Meteor. Soc.*, **80**, 407–420, doi:10.1175/1520-0477(1999)080<0407:TNGD>2.0.CO;2.

Hoffman, R. N., and S. M. Leidner, 2005: An introduction to the near-real-time QuikSCAT data. *Wea. Forecasting*, **20**, 476–493, doi:10.1175/WAF841.1.

Holland, G. J., 1983a: Angular momentum transports in tropical cyclones. *Quart. J. Roy. Meteor. Soc.*, **109**, 187–209, doi:10.1002/qj.49710945909.

——, 1983b: Tropical cyclone motion: Environmental interaction plus a beta effect. *J. Atmos. Sci.*, **40**, 328–342, doi:10.1175/1520-0469(1983)040<0328:TCMEIP>2.0.CO;2.

——, 1984: Tropical cyclone motion: A comparison of theory and observation. *J. Atmos. Sci.*, **41**, 68–75, doi:10.1175/1520-0469(1984)041<0068:TCMACO>2.0.CO;2.

Hristova-Veleva, S. M., and Coauthors, 2013: Revealing the winds under the rain. Part I: Passive microwave rain retrievals using a new observation-based parameterization of subsatellite rain variability and intensity—Algorithm description. *J. Appl. Meteor. Climatol.*, **52**, 2828–2848, doi:10.1175/JAMC-D-12-0237.1.

Jarvinen, B. R., C. J. Neumann, and M. A. S. Davis, 1984: A tropical cyclone data tape for the North Atlantic Basin, 1886–1983: Contents, limitations, and uses. NOAA Tech. Memo. 22, NWS/NHC, Miami, FL, 21 pp. [Available online at http://www.nhc.noaa.gov/pdf/NWS-NHC-1988-22.pdf.]

Jiang, H., E. M. Ramirez, and D. J. Cecil, 2013: Convective and rainfall properties of tropical cyclone inner cores and rainbands from 11 years of TRMM data. *Mon. Wea. Rev.*, **141**, 431–450, doi:10.1175/MWR-D-11-00360.1.

Jones, R. W., 1977: Vortex motion in a tropical cyclone model. *J. Atmos. Sci.*, **34**, 1518–1527, doi:10.1175/1520-0469(1977)034<1518:VMIATC>2.0.CO;2.

Jorgensen, D. P., E. J. Zipser, and M. A. LeMone, 1985: Vertical motions in intense hurricanes. *J. Atmos. Sci.*, **42**, 839–856, doi:10.1175/1520-0469(1985)042<0839:VMIIH>2.0.CO;2.

Kaplan, J., and M. DeMaria, 2003: Large-scale characteristics of rapidly intensifying tropical cyclones in the North Atlantic basin. *Wea. Forecasting*, **18**, 1093–1108, doi:10.1175/1520-0434(2003)018<1093:LCORIT>2.0.CO;2.

——, ——, and J. A. Knaff, 2010: A revised tropical cyclone rapid intensification index for the Atlantic and eastern North Pacific basins. *Wea. Forecasting*, **25**, 220–241, doi:10.1175/2009WAF2222280.1.

Kepert, J., 2001: The dynamics of boundary layer jets within the tropical cyclone core. Part I: Linear theory. *J. Atmos. Sci.*, **58**, 2469–2484, doi:10.1175/1520-0469(2001)058<2469:TDOBLJ>2.0.CO;2.

Klotz, B. W., and E. W. Uhlhorn, 2014: Improved stepped frequency microwave radiometer tropical cyclone surface winds in heavy precipitation. *J. Atmos. Oceanic Technol.*, **31**, 2392–2408, doi:10.1175/JTECH-D-14-00028.1.

——, and H. Jiang, 2016: Global composites of surface wind speeds in tropical cyclones based on a 12 year scatterometer database. *Geophys. Res. Lett.*, **43**, 10 480–10 488, doi:10.1002/2016GL071066.

Knabb, R. D., J. R. Rhome, and D. P. Brown, 2011: Tropical cyclone report: Hurricane Katrina. National Hurricane Center. [Available online at http://www.nhc.noaa.gov/data/tcr/.]

Knaff, J. A., M. DeMaria, D. A. Molenar, C. R. Sampson, and M. G. Seybold, 2011: An automated, objective, multiple-satellite platform tropical cyclone surface wind analysis. *J. Appl. Meteor. Climatol.*, **50**, 2149–2166, doi:10.1175/2011JAMC2673.1.

Kossin, J. P., J. A. Knaff, H. I. Berger, D. C. Herndon, T. A. Cram, C. S. Velden, R. J. Murnane, and J. D. Hawkins, 2007: Estimating hurricane wind structure in the absence of aircraft reconnaissance. *Wea. Forecasting*, **22**, 89–101, doi:10.1175/WAF985.1.

Kuo, H.-L., 1969: Motions of vortices and circulating cylinder in shear flow with friction. *J. Atmos. Sci.*, **26**, 390–398, doi:10.1175/1520-0469(1969)026<0390:MOVACC>2.0.CO;2.

Landsea, C., and J. Franklin, 2013: Atlantic hurricane database uncertainty and presentation of a new database format. *Mon. Wea. Rev.*, **141**, 3576–3592, doi:10.1175/MWR-D-12-00254.1.

Lonfat, M., F. D. Marks Jr., and S. S. Chen, 2004: Precipitation distribution in tropical cyclones using the Tropical Rainfall Measuring Mission (TRMM) Microwave Imager: A global perspective. *Mon. Wea. Rev.*, **132**, 1645–1660, doi:10.1175/1520-0493(2004)132<1645:PDITCU>2.0.CO;2.

Lorsolo, S., and A. Aksoy, 2012: Wavenumber analysis of azimuthally distributed data: Assessing maximum allowable gap size. *Mon. Wea. Rev.*, **140**, 1945–1956, doi:10.1175/MWR-D-11-00219.1.

Mai, M., B. Zhang, X. Li, P. Hwang, and J. A. Zhang, 2016: Application of AMSR-E and AMSR2 low-frequency channel brightness temperature data for hurricane wind retrievals. *IEEE Trans. Geosci. Remote Sens.*, **54**, 4501–4512, doi:10.1109/TGRS.2016.2543502.

Marks, F. D., 1985: Evolution of the structure of precipitation in Hurricane Allen (1980). *Mon. Wea. Rev.*, **113**, 909–930, doi:10.1175/1520-0493(1985)113<0909:EOTSOP>2.0.CO;2.

——, R. A. Houze Jr., and J. F. Gamache, 1992: Dual-aircraft investigation of the inner core of Hurricane Norbert. Part I: Kinematic structure. *J. Atmos. Sci.*, **49**, 919–942, doi:10.1175/1520-0469(1992)049<0919:DAIOTI>2.0.CO;2.

Miller, B. I., 1958: Rainfall rates in Florida hurricanes. *Mon. Wea. Rev.*, **86**, 258–264, doi:10.1175/1520-0493(1958)086<0258:RRIFH>2.0.CO;2.

Molinari, J., and D. Vollaro, 2010: Rapid intensification of a sheared tropical storm. *Mon. Wea. Rev.*, **138**, 3869–3885, doi:10.1175/2010MWR3378.1.

Montgomery, M. T., S. V. Nguyen, R. K. Smith, and J. Persing, 2009: Is WISHE essential for tropical cyclone intensification? *Quart. J. Roy. Meteor. Soc.*, **135**, 1697–1714, doi:10.1002/qj.459.

——, J. A. Zhang, and R. K. Smith, 2014: An analysis of the observed low-level structure of rapidly intensifying and mature hurricane Earl (2010). *Quart. J. Roy. Meteor. Soc.*, **140**, 2132–2146, doi:10.1002/qj.2283.

Mueller, K. J., M. DeMaria, J. A. Knaff, J. P. Kossin, and T. H. Vonder Haar, 2006: Objective estimation of tropical cyclone wind structure from infrared satellite data. *Wea. Forecasting*, **21**, 990–1005, doi:10.1175/WAF955.1.

Pálmen, E., and H. Riehl, 1957: Budget of angular momentum and energy in tropical cyclones. *J. Meteor.*, **14**, 150–159, doi:10.1175/1520-0469(1957)014<0150:BOAMAE>2.0.CO;2.

Powell, M. D., 1980: Evaluations of diagnostic marine boundary-layer models applied to hurricanes. *Mon. Wea. Rev.*, **108**, 757–766, doi:10.1175/1520-0493(1980)108<0757:EODMBL>2.0.CO;2.

——, and S. H. Houston, 1996: Hurricane Andrew's landfall in south Florida. Part II: Surface wind fields and potential real-time applications. *Wea. Forecasting*, **11**, 329–349, doi:10.1175/1520-0434(1996)011<0329:HALISF>2.0.CO;2.

——, ——, L. R. Amat, and N. Morisseau-Leroy, 1998: The HRD real-time hurricane wind analysis system. *J. Wind Eng. Ind. Aerodyn.*, **77–78**, 53–64, doi:10.1016/S0167-6105(98)00131-7.

——, P. J. Vickery, and T. Reinhold, 2003: Reduced drag coefficient for high wind speeds in tropical cyclones. *Nature*, **422**, 279–283, doi:10.1038/nature01481.

Rappaport, E. N., and Coauthors, 2009: Advances and challenges at the National Hurricane Center. *Wea. Forecasting*, **24**, 395–419, doi:10.1175/2008WAF2222128.1.

Reasor, P. D., and M. D. Eastin, 2012: Rapidly intensifying Hurricane Guillermo (1997). Part II: Resilience in shear. *Mon. Wea. Rev.*, **140**, 425–444, doi:10.1175/MWR-D-11-00080.1.

——, M. T. Montgomery, and L. D. Grasso, 2004: A new look at the problem of tropical cyclones in vertical shear flow: Vortex resiliency. *J. Atmos. Sci.*, **61**, 3–22, doi:10.1175/1520-0469(2004)061<0003:ANLATP>2.0.CO;2.

——, R. Rogers, and S. Lorsolo, 2013: Environmental flow impacts on tropical cyclone structure diagnosed from airborne Doppler radar composites. *Mon. Wea. Rev.*, **141**, 2949–2969, doi:10.1175/MWR-D-12-00334.1.

Rodgers, E. B., S. W. Chung, and H. F. Pierce, 1994: A satellite observational and numerical study of precipitation characteristics in western North Atlantic tropical cyclones. *J. Appl. Meteor.*, **33**, 129–139, doi:10.1175/1520-0450(1994)033<0129:ASOANS>2.0.CO;2.

Rogers, R., and E. Uhlhorn, 2008: Observations of the structure and evolution of surface and flight-level wind asymmetries in Hurricane Rita (2005). *Geophys. Res. Lett.*, **35**, L22811, doi:10.1029/2008GL034774.

——, P. D. Reasor, and J. A. Zhang, 2015: Multiscale structure and evolution of Hurricane Earl (2010) during rapid intensification. *Mon. Wea. Rev.*, **143**, 536–562, doi:10.1175/MWR-D-14-00175.1.

Rossby, C. G., 1948: On the displacement and intensity change of atmospheric vortices. *J. Mar. Res.*, **7**, 175–187.

Schade, L. R., and K. A. Emanuel, 1999: The ocean's effect on the intensity of tropical cyclones: Results from a simple coupled atmosphere–ocean model. *J. Atmos. Sci.*, **56**, 642–651, doi:10.1175/1520-0469(1999)056<0642:TOSEOT>2.0.CO;2.

Shapiro, L. J., 1983: The asymmetric boundary layer flow under a translating hurricane. *J. Atmos. Sci.*, **40**, 1984–1998, doi:10.1175/1520-0469(1983)040<1984:TABLFU>2.0.CO;2.

Smith, R. K., M. T. Montgomery, and S. V. Nguyen, 2009: Tropical cyclone spin-up revisited. *Quart. J. Roy. Meteor. Soc.*, **135**, 1321–1335, doi:10.1002/qj.428.

Stiles, B. W., and R. S. Dunbar, 2010: A neural network technique for improving the accuracy of scatterometer winds in rainy conditions. *IEEE Trans. Geosci. Remote Sens.*, **48**, 3114–3122, doi:10.1109/TGRS.2010.2049362.

——, and Coauthors, 2010: Obtaining accurate ocean surface winds in hurricane conditions: A dual-frequency scatterometry approach. *IEEE Trans. Geosci. Remote Sens.*, **48**, 3101–3113, doi:10.1109/TGRS.2010.2045765.

——, R. E. Danielson, W. L. Poulsen, M. J. Brennan, S. Hristova-Veleva, T.-P. Shen, and A. G. Fore, 2014: Optimized tropical cyclone winds from QuikSCAT: A neural network approach. *IEEE Trans. Geosci. Remote Sens.*, **52**, 7418–7434, doi:10.1109/TGRS.2014.2312333.

Tao, C., and H. Jiang, 2015: Distributions of shallow to very deep precipitation/convection in rapidly intensifying tropical cyclones. *J. Climate*, **28**, 8791–8824, doi:10.1175/JCLI-D-14-00448.1.

——, ——, and J. Zawislak, 2017: The relative importance of stratiform and convective rainfall in rapidly intensifying tropical cyclones. *Mon. Wea. Rev.*, **145**, 795–809, doi:10.1175/MWR-D-16-0316.1.

Thomsen, G. L., R. K. Smith, and M. T. Montgomery, 2015: Tropical cyclone flow asymmetries induced by a uniform flow revisited. *J. Adv. Model. Earth Syst.*, **5**, 382–405.

Ueno, M., and M. Kunii, 2009: Some aspects of azimuthal wavenumber-one structure of typhoons represented in the JMA operational mesoscale analyses. *J. Meteor. Soc. Japan*, **87**, 615–633, doi:10.2151/jmsj.87.615.

——, and K. Bessho, 2011: A statistical analysis of near-core surface wind asymmetries in typhoons obtained from QuikSCAT data. *J. Meteor. Soc. Japan*, **89**, 225–241, doi:10.2151/jmsj.2011-304.

Uhlhorn, E. W., and P. G. Black, 2003: Verification of remotely sensed sea surface winds in hurricanes. *J. Atmos. Oceanic Technol.*, **20**, 99–116, doi:10.1175/1520-0426(2003)020<0099:VORSSS>2.0.CO;2.

——, and D. S. Nolan, 2012: Observational undersampling in tropical cyclones and implications for estimated intensity. *Mon. Wea. Rev.*, **140**, 825–840, doi:10.1175/MWR-D-11-00073.1.

——, P. G. Black, J. L. Franklin, M. Goodberlet, J. Carswell, and A. S. Goldstein, 2007: Hurricane surface wind measurements from an operational stepped frequency microwave radiometer. *Mon. Wea. Rev.*, **135**, 3070–3085, doi:10.1175/MWR3454.1.

——, B. W. Klotz, T. Vukicevic, P. D. Reasor, and R. F. Rogers, 2014: Observed hurricane wind speed asymmetries and relationships to motion and environmental shear. *Mon. Wea. Rev.*, **142**, 1290–1311, doi:10.1175/MWR-D-13-00249.1.

Velden, C., and Coauthors, 2006: The Dvorak tropical cyclone intensity estimation technique: A satellite-based method that has endured for over 30 years. *Bull. Amer. Meteor. Soc.*, **87**, 1195–1210, doi:10.1175/BAMS-87-9-1195.

Vukicevic, T., E. Uhlhorn, P. Reasor, and B. Klotz, 2014: A novel multiscale intensity metric for evaluation of tropical cyclone intensity forecasts. *J. Atmos. Sci.*, **71**, 1292–1304, doi:10.1175/JAS-D-13-0153.1.

Willoughby, H. E., F. D. Marks Jr., and R. J. Feinberg, 1984: Stationary and moving convective bands in hurricanes. *J. Atmos.*

Sci., **41**, 3189–3211, doi:10.1175/1520-0469(1984)041<3189:SAMCBI>2.0.CO;2.

Wingo, M. T., and D. J. Cecil, 2010: Effects of vertical wind shear on tropical cyclone precipitation. *Mon. Wea. Rev.*, **138**, 645–662, doi:10.1175/2009MWR2921.1.

Zagrodnik, J. P., and H. Jiang, 2014: Rainfall, convection, and latent heating distributions in rapidly intensifying tropical cyclones. *J. Atmos. Sci.*, **71**, 2789–2809, doi:10.1175/JAS-D-13-0314.1.

Zhang, J. A., and E. W. Uhlhorn, 2012: Hurricane sea surface inflow angle and an observation-based parametric model. *Mon. Wea. Rev.*, **140**, 3587–3605, doi:10.1175/MWR-D-11-00339.1.

——, R. F. Rogers, P. D. Reasor, E. W. Uhlhorn, and F. D. Marks, 2013: Asymmetric hurricane boundary layer structure from dropsonde composites in relation to environmental vertical wind shear. *Mon. Wea. Rev.*, **141**, 3968–3984, doi:10.1175/MWR-D-12-00335.1.